

Escape times across the golden Cantorus of the standard map

N. Miguel, C. Simó and A. Veiuro
Departament de Matemàtiques i Informàtica
Universitat de Barcelona (UB)
Gran Via de les Corts Catalanes 585, 08007 Barcelona, Spain

February 7, 2022

Abstract

We consider the Chirikov standard map for values of the parameter larger than but close to Greene's k_G . We investigate the dynamics near the golden Cantorus and we study escape rates across it. Mackay [17, 19] described the behaviour of the mean of the number of iterates $\langle N_k \rangle$ to cross the Cantorus when $k \rightarrow k_G$ and showed that there exists $B < 0$ so that $\langle N_k \rangle (k - k_G)^B$ becomes 1-periodic in a suitable logarithmic scale. The numerical explorations here give evidence of the shape of this periodic function and of the relation between the escape rates and the evolution of the stability islands close to the Cantorus.

Dedicated to the memory of Alexey V. Borisov

1 Introduction

Professor Borisov has done an impressive task in Dynamical systems and related topics. He did an excellent work on the dynamics of rigid bodies and falling bodies, on the dynamics of points masses and vortices in surfaces, on integrable, nonintegrable and nonholonomic systems, on chaotic and regular motions, etc. Furthermore he did an impacting work as cofounder and editor-in-chief of Regular and Chaotic Dynamics. His unexpected sudden death was a shock for many people in Dynamical Systems.

In the present paper we discuss a topic strongly related to the passage from regular to chaotic dynamics in a classical problem.

Any reasonable attempt of describing the phase space transport properties of a given dynamical system must take into account the interaction between the main invariant objects and their evolution with respect to the sensitive parameters. Clearly, the breakdown of codimension one invariant manifolds changes the global transport properties of the system.

In the simple setting of twist area-preserving maps (twist APMs) of the cylinder, the rotational invariant curves (RIC) confine the dynamics. If a large enough perturbation acts on the map so that a RIC of a given rotation number is destroyed, a remnant Aubry-Mather set, with the same rotation number persists, [23]. Since these sets have a Cantor structure with gaps usually one refers to them as Cantori. In particular, orbits can leak through these Cantori, but one may expect the transit time to be extremely large if the gaps are small.

The purpose of this paper is to perform a quantitative study of the escape rates across a Cantorus. Concretely, we consider the Chirikov standard map [5] $M_k : \mathbb{S}^1 \times \mathbb{R} \rightarrow \mathbb{S}^1 \times \mathbb{R}$ given by

$$M_k : \begin{pmatrix} x \\ y \end{pmatrix} \mapsto \begin{pmatrix} \bar{x} \\ \bar{y} \end{pmatrix} = \begin{pmatrix} x + \bar{y} \\ y + \frac{k}{2\pi} \sin(2\pi x) \end{pmatrix}, \quad (1)$$

and we investigate the transport properties for values of the parameter k larger than but close to Greene's parameter $k_G \approx 0.971635406$, that is through the remnant Cantor set after the breakdown of the RIC with golden rotation number $\omega = (\sqrt{5}-1)/2$. **There is a strong numerical evidence supporting the fact that the RIC with golden rotation number is the last one to be destroyed when increasing $k \geq 0$. On the other hand, the golden frequency has optimal Diophantine properties among real numbers. Even though it has not been formally proved, we implicitly assume this fact in our explorations, as we consider values of k near k_G and we use the arithmetic properties of the golden number to explore the dynamics. Our numerical work also supports this evidence.**

Certainly this is a classical problem that has been the topic of many previous studies. One of the goals of this paper is to overview the results available while providing new numerical evidences. In particular, special emphasis is made on the fine structure of the phase space close to the destruction of the golden invariant curve. The careful computations reported in this work give a clear evidence of the role of the tiny islands in the escape rates through the Cantorus. The paper is organised as follows.

In Sect. 2 we review the main features of the so-called Greene-MacKay renormalisation theory. In particular, we recall the definition and the main features of the dynamics of the renormalisation operator for golden invariant curves in APMs.

In Sect. 3 we link the renormalisation operator with the phase space of the standard family of maps. In particular, we choose suitable scalings close to the golden Cantorus with the aid of the position of periodic points whose rotation number is an approximant of the golden mean.

Sect. 4 is devoted to the study of the geometry of the phase space close to the Cantorus. We pay special attention to the local dynamics around elliptic ($|\text{tr}| < 2$) and/or reflection-hyperbolic ($\text{tr} < -2$) periodic orbits whose rotation number is an approximant of the golden mean, and to the area of the stability domain that surrounds them, if any¹. We argue that these objects are key to explain the transport rates across the Cantorus.

In Sect. 5 we present a numerical study of escape rates based on massive simulations. The available theoretical frameworks predict an inverse potential behaviour of the escape rates in a parameter that measures the distance to the breakdown $\Delta k = k - k_G$, $k > k_G$, times some periodic fluctuations in logarithmic scale of Δk . We show the corresponding periodic function and link it to the existence and evolution of the islands of stability we dealt with in Sect. 4. We finish by studying the probability law of the escape rates and its behaviour as k tends to k_G .

Finally, in Sect. 6 we summarize the results obtained and mention future research directions that can lead to a better comprehension of the escape rates through Cantori.

To end this introduction, we note that some of the computations that we report in this paper require multiprecision arithmetics. We have used Pari/GP [2] to this end.

¹For a q -periodic point of (1), the symbol tr refers to the trace of the differential matrix of M_k^q evaluated at the periodic point.

2 A review of renormalisation for invariant curves

Renormalisation in dynamical systems is a tool to deal with asymptotic self-similarity. In the discrete context, this is done by studying the system in smaller scales, by considering a conveniently scaled version of the original phase variables, and in longer scales of time. Kadanoff and Shenker [14] were the first to introduce a renormalisation approach to deal with RIC. Later, MacKay [19, 17] refined the idea by linking in a more precise way the renormalisation operator and RIC, by taking into account the pioneering work of Greene [12]. This approach is usually referred to as Greene-MacKay renormalisation theory. This section is a compendium of well known facts about the Greene-Mackay renormalisation theory for invariant curves of twist APMs.

2.1 Renormalisation for invariant curves

Briefly explained the Greene-Mackay renormalisation scheme consists in the following. Consider an area-preserving twist map F of the cylinder $\mathbb{S}^1 \times \mathbb{R}$ and assume that it has a RIC with rotation number $\rho \in [0, 1)$. Denote by \bar{F} a lift of F to the plane. Let (x_0, y_0) be a point of the RIC, denote $\bar{F}^n(x_0, y_0)$ as (x_n, y_n) and consider any sequence $\{n_j/m_j\}_j$ of rationals tending to ρ as $j \rightarrow \infty$. Then,

$$\pi_1 \bar{F}^{m_j} R^{n_j}(x_0, y_0) = x_{m_j} - n_j \rightarrow x_0,$$

where $\pi_1(x, y) = x$ is the projection onto the first variable and $R(x, y) = (x - 1, y)$ is the back rotation by one period around the cylinder. This suggests that the study of the dynamics near the invariant curve can be approached by considering a sequence of maps of the form $\Lambda \bar{F}^{m_j} R^{n_j} \Lambda^{-1}$, where Λ is a change of variables that is meant to scale the phase space and zoom in regions chosen according to the relative positions of periodic orbits whose periods correspond to two consecutive best approximants of ρ . The setting introduced in [19, 17] consists in embedding this sequence as iterates of a suitable renormalisation operator in a suitable functional space.

The map F is periodic in $x \in \mathbb{S}^1$, that is, it commutes with R . To preserve periodicity in $x \in \mathbb{S}^1$ the renormalisation operator is defined on commuting pairs (U, T) , that is, it acts on a pair U, T of real orientation-preserving diffeomorphisms of the plane that are assumed to commute where the compositions UT and TU are defined. Concretely, one introduces the following family of renormalisation operators:

$$\mathcal{R}_m(U, T) = \Lambda(T, T^m U) \Lambda^{-1}, \quad m \in \mathbb{Z},$$

where $\Lambda(A, B) \Lambda' = (\Lambda A \Lambda', \Lambda B \Lambda')$ for arbitrary changes of variable (Λ, Λ') .

To investigate the phase space structure near the RIC one considers the commuting pair (R, \bar{F}) and perform iterates under a suitable sequence (a sequence of m values) of renormalisation operators \mathcal{R}_m . The choice of the sequence of m 's is related to the arithmetic properties of $\rho \in [0, 1)$. Consider the continuous fraction expansion

$$\rho = [l_0, l_1, l_2, \dots] = \frac{1}{l_0 + \frac{1}{l_1 + \dots}}$$

and recall that the best approximants of ρ are p_k/q_k where $p_0 = 0$, $q_0 = p_1 = 1$, $q_1 = l_0$ and $p_k = l_{k-1}p_{k-1} + p_{k-2}$, $q_k = l_{k-1}q_{k-1} + q_{k-2}$, for $k \geq 2$. It follows from properties of continued fraction expansions that

$$\mathcal{R}_{l_j} \cdots \mathcal{R}_{l_0}(R, \bar{F}) = \Lambda_{j+1}(\bar{F}^{q_j} R^{p_j}, \bar{F}^{q_{j+1}} R^{p_{j+1}}) \Lambda_{j+1}^{-1},$$

where Λ_{j+1} is the composition of successive shifted scalings. We will assume that the sequence Λ_j tends to a limit Λ , as this is a necessary requirement for the existence of fixed points of the renormalisation operator. Hence the phase space structure close to the RIC of rotation number ρ is encoded in the first component $\Lambda F^{q_n} R^{p_n} \Lambda^{-1}$ of $\mathcal{R}_{l_n} \cdots \mathcal{R}_{l_0}(R, \bar{F})$. The following properties hold:

1. Let us briefly recall the definition of rotation number for commuting pairs (see [19]): a point (x, y) has rotation number ρ under (U, T) if, for any sequence $p_n/q_n \rightarrow \rho$ as $n \rightarrow \infty$, $0 < p_n < q_n$, $q_n \rightarrow \infty$ as $n \rightarrow \infty$, the first component of $U^{p_n} T^{q_n}(x, y)/q_n \rightarrow 0$ as $n \rightarrow \infty$. In particular, a p/q periodic orbit of (U, T) is a fixed point of $U^p T^q$.

Then, as noticed in [19], if a map F has an orbit with rotation number $\rho = [l_0, l_1, l_2, \dots]$, one finds that $\mathcal{R}_{l_n} \cdots \mathcal{R}_{l_0}(R, \bar{F})$ has an orbit with rotation number $\rho' = [l_{n+1}, l_{n+2}, \dots]$.

In particular, if $\rho = \omega = (\sqrt{5} - 1)/2 = [1, 1, 1, \dots]$ and p_j/q_j are its approximants (hence quotients of successive Fibonacci numbers) then:

- (a) if F has an orbit with rotation number p_j/q_j , then $\mathcal{R}_1(R, \bar{F})$ has an orbit with rotation number p_{j-1}/q_{j-1} , the previous approximant; and
 - (b) if F has a golden RIC (resp. Cantorus) then the first component of $\mathcal{R}_1^n(R, \bar{F})$, $n \geq 1$, defines a map of the annulus that has a golden RIC (resp. Cantorus).
2. The linear stability of a q -periodic orbit is determined by the trace $\tau = \text{tr} DF^q(x_0, y_0)$, where (x_0, y_0) is any point in the orbit. Then, if F has an orbit with rotation number $\rho = p/q$ with τ as trace, then the corresponding periodic orbit with rotation number $\rho' = p'/q' = q/p - l_0$ of $\mathcal{R}_1(R, \bar{F})$ has also trace τ .

2.2 Dynamics of the renormalisation operator \mathcal{R}_1

As commented above, the phase space structure close to a golden RIC is encoded in the iterates of the operator

$$\mathcal{R}_1(U, T) = \Lambda(T, TU)\Lambda^{-1},$$

where $\Lambda : \mathbb{R}^2 \rightarrow \mathbb{R}^2$ will be assumed to be of the form

$$\Lambda : \begin{pmatrix} \xi \\ \eta \end{pmatrix} \mapsto \begin{pmatrix} \alpha\xi + c \\ \beta\eta + p(\xi) \end{pmatrix} \quad (2)$$

being $\alpha, \beta \in \mathbb{R}$ the phase scaling factors, $c \in \mathbb{R}$ is a constant and $p(x)$ is a real polynomial that we shall consider to be of degree 3. See the comments on this assumption in Sect. 3.1. The dynamics of the renormalisation operator \mathcal{R}_1 was first studied in [19, 17], where the most important features of its phase space were described. Some of them have been already proven, but some essential questions that have a reasonable conjectural solution remain still open, [16].

Below we consider area and orientation preserving maps of the cylinder with zero flux. We recall that, geometrically, the flux is simply the net area between an embedded circle wrapping once around the cylinder and its image. More formally, let F be a lift of a map f of the cylinder and denote by $(\bar{x}, \bar{y}) = F(x, y)$ the image of a point $z = (x, y)$. Denote by $T(z) = (x + 1, y)$ and choose a base point $z_0 = (x_0, y_0)$ in the cylinder. Then the flux of f is given by the difference of path integrals $\int_{z_0}^{T(z_0)} \lambda - \int_{z_0}^{z_0} \lambda$ where $\lambda = \bar{y}d\bar{x} - ydx$. Note that λ is a closed 1-form, hence Stokes theorem implies that the integrals do not depend on the chosen path on the cylinder. See, for example, [11, 25] for further details.

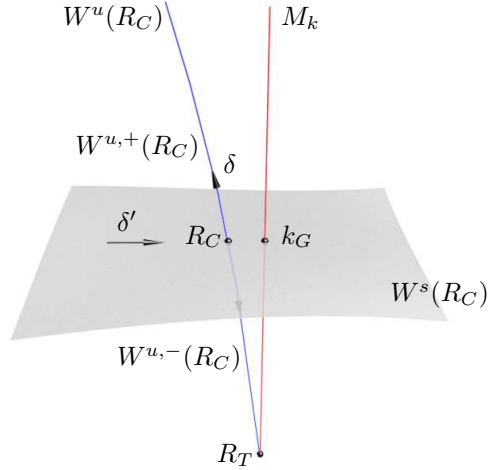


Figure 1: Sketch of the conjectured skeleton of \mathcal{R}_1 .

Essentially, when acting on the area preserving zero flux class of maps, the most relevant part of the phase space of \mathcal{R}_1 is characterised by the existence of two fixed points:

1. The *trivial* fixed point R_T which is an integrable linear shear

$$R_T \begin{pmatrix} x \\ y \end{pmatrix} = \begin{pmatrix} x + (\omega + 1)y + \omega \\ y \end{pmatrix}.$$

It is an attracting fixed point in the area-preserving class of maps, see [19]. All the periodic orbits in the phase space of R_T are parabolic ($\tau = 2$).

2. The *critical* fixed point R_C which is a map having a critical golden RIC. It is a saddle fixed point with a single unstable eigenvalue δ . All elliptic approximating orbits of R_C have the same trace, $\tau = \tau^*$, see (6). By approximating orbit we refer to periodic orbits having as rotation number an approximant of the golden number ω .

The fixed point R_C was numerically computed in [19] together with a 1-parameter family of maps contained in $W^u(R_C)$, giving a strong numerical evidence of its saddle linear behaviour. The existence of R_C was finally proven in [1] and the fact that it was hyperbolic with a single unstable direction with eigenvalue δ was proven in [15].

Summarizing, it was conjectured in [19, 17] that the dynamics in a neighborhood of these two fixed points was as sketched in Fig. 1. In this figure we also added in red the conjectured relative position of the standard family, M_k , in this functional phase space.

Note that $W^s(R_C)$ is a codimension one invariant manifold of maps with a critical golden RIC, so locally separates maps with a golden RIC and maps with a golden Cantorus. Hence $W^u(R_C) \setminus \{R_C\}$ has two components. Denote the one that consists in maps with a golden RIC as $W^{u,-}(R_C)$, and the other component as $W^{u,+}(R_C)$. A conjecture related to Fig. 1 that is still open is if $W^{u,-}(R_C)$ is a heteroclinic connection between R_T and R_C , that is, if this whole branch is contained in the basin of attraction of the trivial fixed point R_T . In fact, it was the original motivation of the renormalisation operator: the goal was to prove that all maps with a golden RIC **with a smooth conjugacy to a rotation** converged to R_T under \mathcal{R}_1 **and to understand how golden RICs break**. For results in this direction one can see, for instance, [13, 31, 32].

3 The standard family in the phase space of \mathcal{R}_1

All numerical experiments dealing with approximating periodic orbits of the golden RIC carried out for the standard map suggest that this family of maps is close to $W^u(R_C)$, as depicted in Fig. 1. Namely, the approximations of the phase space scalings α and β (2) and the eigenvalue δ given in [1, 15] in the proofs of the existence and hyperbolicity of R_C agree with the corresponding quantities found experimentally in the standard map [14, 17, 19]. Through the text we shall refer to the Birkhoff periodic orbits having rotation number the n th best approximant p_n/q_n of the golden frequency as n th approximating orbits.

For the numerical experiments we shall present it will be important to recall how the constants α, β and δ were first obtained and the most accurate values available in the literature. Here one uses that all monotone elliptic (with $|\text{tr}| < 2$) and reflection-hyperbolic periodic orbits (with $\text{tr} < -2$) in the standard map (1) have a point on the symmetry line $\{x = 1/2\}$, that is a line of fixed points of the involution $(x, y) \mapsto (-x, y + k \sin(2\pi x)/2\pi)$, see [19]. We recall, see for example [11], that an orbit $\{(x_k, y_k)\}_{k \in \mathbb{Z}}$ of a twist map is said to be monotone (or Birkhoff) if the sequence $\{x_k\}_{k \in \mathbb{Z}}$ is cyclically ordered, that is, if $x_k \leq x_{j+p}$ for $k, j, p \in \mathbb{Z}$ then $x_{k+1} \leq x_{j+1+p}$. Let k_j denote the value of the parameter at which the j th elliptic approximating orbit is at a period-doubling bifurcation², that is, $\text{tr} = -2$.

Given k , let $y_n(k)$ denote the y -coordinate of the position of the point of the n th elliptic or reflection-hyperbolic approximating orbit on the symmetry line $\{x = 1/2\}$ and, if n is odd (resp. even), let $x_n(k)$ denote the x -coordinate of the point in the n th hyperbolic approximating orbit closest to the right (resp. left) to $\{x = 1/2\}$. The standard map symmetries imply that the points in the hyperbolic orbit that are the closest to the left or to the right to the symmetry line are equidistant from the symmetry line. We note that:

1. The eigenvalue δ was first approximated in [19] as the inverse of the convergence rate of the sequence $\{k_j\}_j$ towards k_G . In [15] it was obtained

$$\lim_{n \rightarrow \infty} \frac{k_n - k_{n-1}}{k_{n+1} - k_n} = \delta \approx 1.62795006498458161676240425734986. \quad (3)$$

2. The phase scaling β is the inverse of the rate of convergence to 0 of the relative distance between consecutive elliptic (or reflection-hyperbolic) approximating orbits on the symmetry line, that is,

$$\lim_{n \rightarrow \infty} \frac{y_n(k_G) - y_{n-1}(k_G)}{y_{n+1}(k_G) - y_n(k_G)} = \beta \approx (-0.32606339662500148530812206358643)^{-1}, \quad (4)$$

and α is the inverse of the rate of convergence to 0 of the relative distance between elliptic (or reflection-hyperbolic) and hyperbolic orbits of the same rotation number

$$\lim_{n \rightarrow \infty} \frac{(x_n(k_G) - 0.5) - (x_{n-1}(k_G) - 0.5)}{(x_{n+1}(k_G) - 0.5) - (x_n(k_G) - 0.5)} = \alpha \approx (-0.70679566917963727816491731416)^{-1}. \quad (5)$$

The previous values for α and β can be found in [1, 15]. We emphasize that they agree with the actual values for the standard map [14, 19].

²We will slightly change this notation in Sect. 4.

3. There are two other constants, τ^* and δ' , that is worth to take into account, see [19, 17]. Let $\text{tr}_j(k) = \text{trace } DM_k^{q_j}(1/2, y_j(k))$. Then,

$$\lim_{n \rightarrow \infty} \text{tr}_n(k_G) = \tau^* \approx 0.999644. \quad (6)$$

Moreover, the rate of convergence of the sequence $\{\text{tr}_j(k_G)\}_j$ is

$$\lim_{n \rightarrow \infty} \frac{\text{tr}_{n+1}(k_G) - \text{tr}_n(k_G)}{\text{tr}_n(k_G) - \text{tr}_{n-1}(k_G)} = \delta' \approx -0.610830 \quad (7)$$

and corresponds to the dominant attraction rate in $W^s(R_C)$.

Clearly, the standard family M_k is not invariant under \mathcal{R}_1 , but it reflects the behaviour of $W^u(R_C)$. Namely, if $k > k_G$ the orbit of M_k under \mathcal{R}_1 will have some iterates close to $W^{u,+}(R_C)$ due to the hyperbolic character of R_C in the functional space. And after some iterates, the maps one obtains behave as maps with a seemingly fully chaotic phase space. If $k < k_G$ then the iterates are conjectured to tend to R_T . And if $k = k_G$, since $M_{k_G} \in W^s(R_C)$, they will tend to R_C under iteration of \mathcal{R}_1 .

We refer to [16] for an explanation of the dynamics of \mathcal{R}_1 , a discussion on the open questions related to the renormalisation operator and its relationship with Greene's criterion [12] and with Olvera and Simó's Obstruction criterion [28].

Note that the previous considerations on \mathcal{R}_1 hold for the RIC with golden rotation number ω . In general, the scaling factors and eigenvalues α, β, δ and δ' , and even τ^* depend strongly on the continued fraction expansion of the rotation number of the RIC under study. Namely, for noble rotation numbers the set of parameters we should eventually find are $\alpha, \beta, \delta, \delta'$ and τ^* , but not necessarily for metallic irrational numbers (those whose quotients in their continued fraction expansion are equal or eventually equal to $a \in \mathbb{N}$, $a > 1$). Moreover, if the corresponding continued fraction expansion is n periodic, one expects the corresponding renormalisation operator to have a critical n -periodic orbit and a set of n different values of τ^* , and of course different scalings. See [3].

3.1 Choice of the successive scalings Λ_j

As commented above, the scalings Λ_j depend on the positions of the approximating periodic orbits. Approximating orbits are not generically on straight horizontal lines, so one can not expect Λ_j to be a diagonal scaling (that is, $c = 0$ and $p(x) = 0$ for all x in (2)), despite this can be achieved in many examples by a suitable coordinate change. But if we assume that we have a preferred symmetry line where all elliptic or reflection-hyperbolic monotone orbits have a point on, we can reduce Λ_j to be of the form (2). For the standard map (1) this symmetry line is $\{x = 1/2\}$. Hence $c = 0$ in (2). For simplicity, we are going to use the coordinate $\xi = x - 1/2$ instead of x .

Let us consider the j th approximant of ω . For a given value of k , the renormalisation iterates of M_k are defined on domains around the golden RIC or golden Cantorus, between the orbits with rotation number p_j/q_j and p_{j+1}/q_{j+1} . The following steps determine the scalings defining the corresponding renormalised domains:

1. Compute the following orbits and points:

- 1.1 The elliptic (or reflection-hyperbolic) orbit on the symmetry line with p_j/q_j as rotation number. Call it P_e^j .
 - 1.2 If j is odd (resp. even), the point in the orbit of P_e^j closest to the right (resp. left) of it ³. Call it Q_e^j .
 - 1.3 The elliptic (or reflection-hyperbolic) orbit on $\{x = 1/2\}$ with p_{j+1}/q_{j+1} as rotation number. Call it P_e^{j+1} . It can be either above or under P_e^j , depending on the parity of j .
 - 1.4 The hyperbolic orbit with p_j/q_j as rotation number⁴. Call the points in this orbit closest to P_e^j to the left and to the right as L_h^j and R_h^j , respectively.
2. Let $p^{(j)}(\xi) = s_1^{(j)}\xi + s_2^{(j)}\xi^2 + s_3^{(j)}\xi^3$ be the cubic interpolating polynomial of the 4 points $L_h^j, P_e^j, R_h^j, Q_e^j$, after moving their abscissas -0.5 , that is, in such a way that the x -coordinate of P_e^j is 0.
 3. Let $d_x^{(j)} = \max(|\pi_1(P_e^j - L_h^j)|, |\pi_1(P_e^j - R_h^j)|)$, and $d_y^{(j)} = |\pi_2(P_e^j - P_e^{j+1})|$, where π_1 and π_2 are the projections onto the first and second variable.

After all these computations, consider the sequence of changes of variables obtained as the composition of, first, scaling around P_e^j by $d_x^{(j)}$ in the x direction and by $d_y^{(j)}$ in the y direction, then subtracting $p^{(j)}(\xi)$ in the second variable and finally shifting the coordinates to translate P_e^j to the origin. This altogether reads (suppressing some dependencies on j to lighten the notation)

$$\Lambda_j : \begin{pmatrix} \xi \\ \eta \end{pmatrix} \mapsto \begin{pmatrix} d_x \xi + 1/2 \\ d_y \eta + \pi_2(P_e^j) + s_1 d_x \xi + s_2 (d_x \xi)^2 + s_3 (d_x \xi)^3 \end{pmatrix} = \begin{pmatrix} x \\ y \end{pmatrix}, \quad (8)$$

and transforms the rectangle $[-1, 1] \times [0, 1]$, where the island is centered in the origin and the next approximant is at $(0, 1)$, into the variables of the standard map, see Figures 2 and 3 for some examples.

- Remark 3.1.*
1. Concerning $d_x^{(j)}$, the symmetries of the standard map imply that, actually $|\pi_1(P_e^j - L_h^j)| = |\pi_1(P_e^j - R_h^j)|$. Hence in the box $[-1, 1] \times [-1, 1]$ we will have $(-1, 0)$ and $(1, 0)$ as hyperbolic fixed points and $(0, 0)$ as elliptic or reflection-hyperbolic fixed point.
 2. The sequences $d_x^{(j)}$ and $d_y^{(j)}$ go to zero geometrically with rates $1/\alpha$ and $1/\beta$, respectively.
 3. The fact that the polynomial $p(\xi)$ has been chosen as cubic is enough [20, 15], since there is numerical evidence that this condition guarantees that after q_j iterates of points in some compact domain around P_e^j they return to the desired domain. **The fact that it is enough to use a cubic polynomial follows because $|\beta| < |\alpha|^4$, see [17] and the values given in (4) and (5).**
 4. We want the renormalised domain close to $\eta = 0$ to be the domain of definition of a map of the cylinder, that is, to be able to identify the segments of points with coordinates $(-1, \eta)$ and $(1, \eta)$ for $|\eta|$ small. To do so, the right branches of the invariant manifolds of $(1, 0)$ should be the same as the right branches of the invariant manifolds of $(-1, 0)$, but horizontally shifted by 2 units. We get this by imposing that $\Lambda_j^{-1}(Q_e^j)$ also lies on $\eta = 0$.

³This point has to be chosen in different sides of the symmetry line depending on the parity due to the fact that two periodic orbits with consecutive approximants as rotation number lie on different sides of the invariant curve or Cantorus.

⁴In the case of the standard map (1), it can be found either on the lines $\{y = 2x\}$ and $\{y = 2x - 1\}$ or in one of them, depending on j .

5. The symmetries of the standard map M_k impose some conditions on the coefficients of the cubic polynomial $p(\xi)$. Express $M_k = I_1 \circ I_2$, $I_1 : (x, y) \mapsto (-x + y, y)$, $I_2 : (x, y) \mapsto (-x, y + k \sin(2\pi x)/2\pi)$. By construction, the points that define the domains of a renormalisation step lie on invariant sets under I_2 that are near the set $\{\xi = x - 1/2 = 0\}$ of fixed points of I_2 . Imposing $y = p(\xi) = s_1\xi + s_2\xi^2 + s_3\xi^3$ to be invariant under I_2 leads to $p(-\xi) = p(\xi) - k \sin(2\pi\xi)/2\pi$ and $s_1 = k/2$, $s_3 = -k\pi^2/3$. Then, for each fixed value of k , the coefficients of $p^{(j)}(\xi)$ are such that

$$\lim_{j \rightarrow \infty} s_1^{(j)} = k/2, \quad \lim_{j \rightarrow \infty} s_3^{(j)} = -\pi^2 k/3. \quad (9)$$

3.2 Iterations of the standard map M_k under the operator \mathcal{R}_1 .

The renormalisation iterates of M_k are defined in the renormalised domains given by Λ_j as derived in Sect. 3.1. In Fig. 2 and Fig. 3 we show the phase space structure of $\mathcal{R}_1^j[M_k] = \Lambda_j^{-1} \circ M_k^{q_j} \circ \Lambda_j$ in $(\xi, \eta) \in [-1, 1] \times [0, 1.2]$ for two different values of the parameter k before and after the breakdown of the golden RIC. We considered an equispaced 512×512 grid and we indicate in light grey those pixels whose center can be considered regular by approximating the maximal Lyapunov exponent. In black, we highlight the positions of the 0/1, 1/2 and 2/3-periodic orbits of $\mathcal{R}_1^j[M_k]$. More concretely,

1. In Fig. 2 we show how does \mathcal{R}_1 act on M_k , for $k = 0.9716 < k_G$. For this value of the parameter it has been proved in [10] the existence of the golden RIC. Hence, as conjectured [17, 19] (recall Fig. 1) we expect the iterates under \mathcal{R}_1 to tend to R_T . In the top left plot we show the dynamics around the golden RIC under M_k^2 . Hence, the 1/2 elliptic periodic orbit of M_k corresponds to the fixed point at the origin and the 2/3 elliptic periodic orbit of M_k becomes the 2-periodic orbit at $(0, 1)$ shown in the plot. In the same plot, we also indicate the points that are going to define the next renormalised domain. The phase space of the renormalised mapping (that is, under M_k^3 between the 2/3 and the 5/8 periodic orbits of M_k , and changing signs both in ξ and η) is shown on the next right plot in the sequence. Successive iterations of the renormalisation operator are shown. From left to right and from top to bottom we show 16 iterates of the renormalisation map, the title in each picture indicates the number of iterate.⁵ Note that, as we iterate, we tend to a more regular phase space and, in fact, for the 17th iterate (not shown), with the resolution used for these plots, we do not detect a single chaotic orbit.
2. Fig. 3 is analogous to Fig. 2 but for $k = 0.98$. We see that phase space of M_k becomes more and more chaotic when performing iterates of \mathcal{R}_1 . This is the expected behaviour once the golden RIC is destroyed, see Fig. 1. To reach a seemingly fully chaotic phase space, with the resolution used in the plots and for $k = 0.98$, one only needs 11 iterates (we show the first 10 iterates of $\mathcal{R}_1[M_k]$).

4 The phase space near a Cantorus

In this section we want to describe the phase space around a broken invariant curve. We consider the golden Cantorus and we study the relative position and relative size of the approximating

⁵For iterates ≥ 14 small chaotic zones are visible by magnifying the plot in the electronic version.

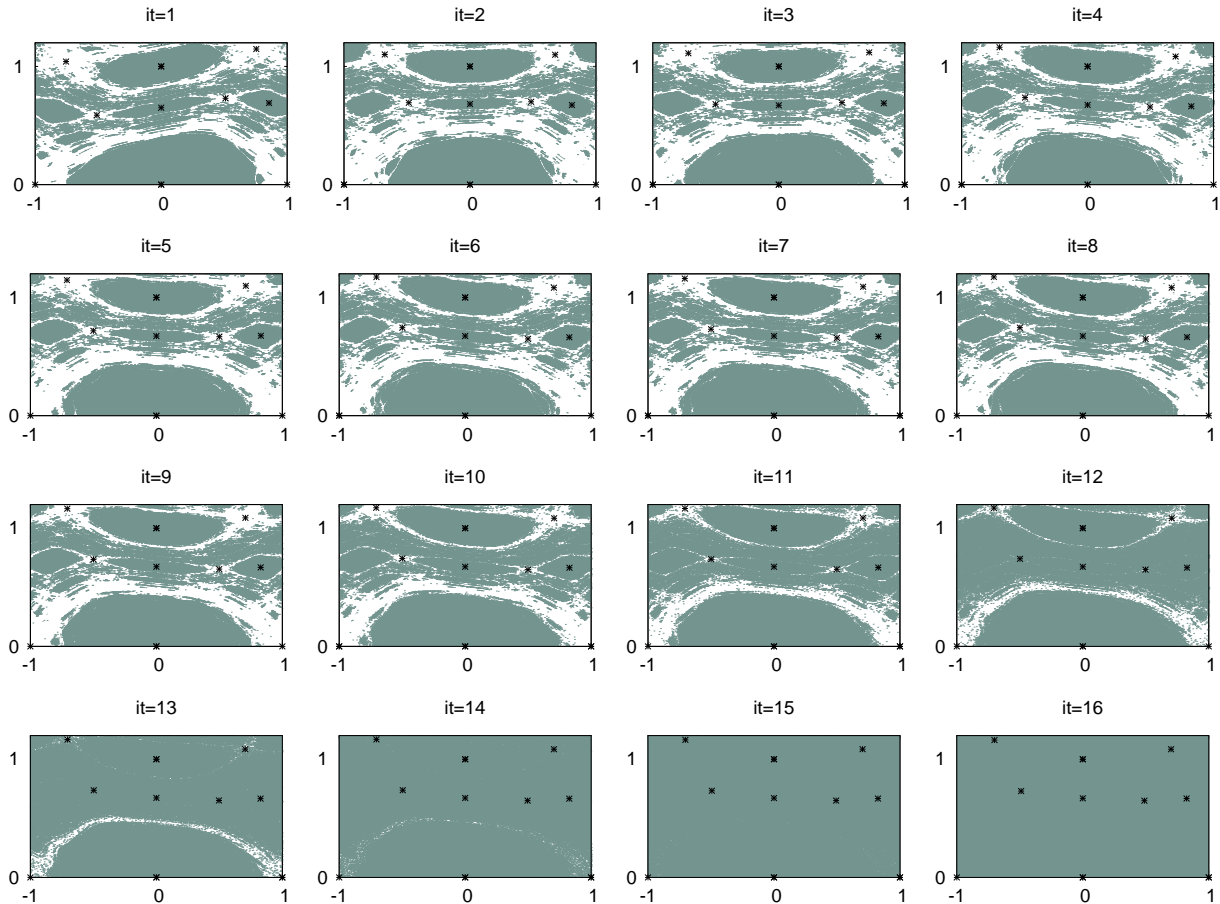


Figure 2: Iterates of M_k , $k = 0.9716 < k_G$ under \mathcal{R}_1 . From left to right and from top to bottom, we show how the consecutive iterates of M_k tend to a regular map.

islands (that is, islands of stability related to the best approximants of the golden rotation number). The renormalisation theory implies that the scaling factors that will allow to relate the renormalised islands are the eigenvalues δ and δ' for the parameter and α and β for the phase variables. First, we provide numerical computations that support that the traces tr_j of the elliptic approximating orbits change monotonically in the parameter. Second, we show that for each fixed k , close enough but larger than k_G , the approximating islands tend, as $j \rightarrow \infty$, to an island with a limit structure, and we show how such island evolves with respect to k in a suitable fundamental domain.

4.1 Numerical study of the local dynamics of elliptic approximating orbits

We consider ranges of k where elliptic periodic orbits evolve from parabolic to the period-doubling bifurcation and we numerically study the dependence of the traces tr_j with respect to k . The numerical studies in [12] suggest that the sequence $\{k_j(-2)\}_j$, of values of k for which the j -approximant elliptic orbit has trace equal to -2 (that is, it bifurcates to reflection-hyperbolic), is monotonically decreasing and $\lim_{j \rightarrow \infty} k_j(-2) = k_G$. The behaviour of $k_j(\tau)$, both as a function of τ and as a sequence $\{k_j(\tau)\}_j$ for each fixed value of $\tau \in [-2, 2)$ is displayed in Fig. 4 left, for $k_j(\tau)$, $j = 1, \dots, 17$. First, the results suggest that the following property holds for M_k .

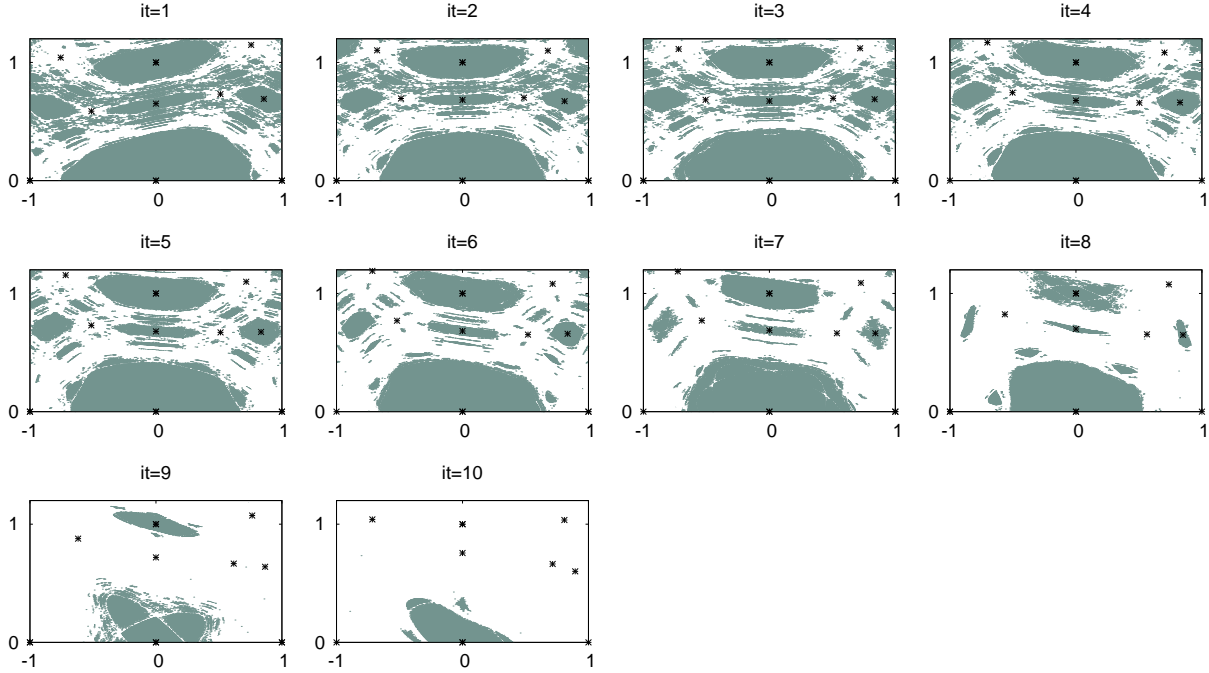


Figure 3: Iterates of M_k , $k = 0.98 > k_G$ under \mathcal{R}_1 . From left to right and from top to bottom, we show how the successive iterates tend to a chaotic map.

Conjecture 1. *The function $k_j(\tau)$ is strictly decreasing in τ , for all $j > 0$.*

Note that if such conjecture holds, the multiplier of the j th elliptic approximating orbit has a full passage through resonances and, in case Greene's criterion holds, that the golden RIC can not reappear after k_G . We remark that we would not expect such monotonicity in cases where RIC can reappear after their destruction, as happens, for instance, in standard-like maps with a two-harmonic potential, see [8, 9, 4, 22]. Other examples where all the RIC are destroyed and then several RIC reappear when increasing a parameter can be found in [6].

On the other hand, in Fig. 4 left, we can also see that, as j increases, the graphs $k_j(\tau)$ tend point-wise to be a constant function. That is,

$$\lim_{j \rightarrow \infty} k_j(\tau) = k_G, \quad \text{if } \tau < 2, \quad (10)$$

Note that (10) includes values of k where the golden RIC still exists, as shown in Fig. 4 left. Here we give evidence for $\tau > -2$, but we also have evidence for some values of τ such that $\tau < -2$. For these values, the sequence $\{k_j(\tau)\}_j$ behaves as in the interval $\tau \in [-2, \tau_-]$, where τ_- is the value of the trace given in (11) below.

The convergence of $\{k_j(\tau)\}_j$ to k_G implies the convergence of the coefficients $s_1^{(j)}$ and $s_3^{(j)}$ of the cubical change of variables (8) to the limit values (9). We checked such convergence by considering convergents $j = 3, \dots, 30$, that is, from the $2/3$ to the $832040/1346269$ elliptic periodic point, and computing $s_i^{(j)}$, $i = 1, 2, 3$, along the sequence $\{k_j(-1)\}_j$ corresponding to the 1:3 resonance of each of the approximating elliptic periodic orbits. We used 75 digits precision to compute the positions P_e^j and the values $k_j(-1)$. The results are summarised in Table 1, where we also report on the rates of convergence and Aitken's delta-squared acceleration is used to obtain better approximations of the limit of each sequence. We note that:

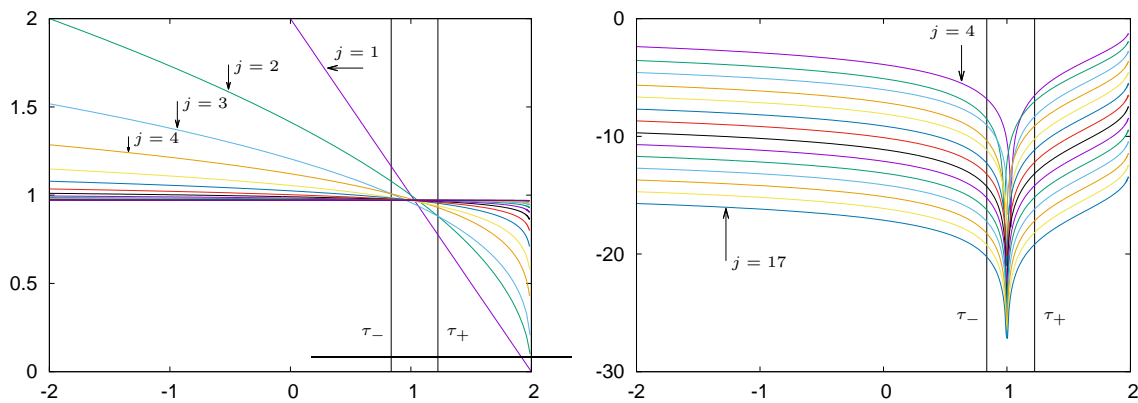


Figure 4: Left: Evolution of the value $k_j(\tau)$, for $\tau \in [-2, 2)$ for $j = 1, \dots, 17$. Right: $\tilde{k}_j(\tau) = \log_\delta |k_j(\tau) - k_G|$ as a function of $\tau \in [-2, 2)$ for $j = 4, \dots, 17$. Here we only show values of j that are visibly equispaced in some ranges of τ . See the text for the definition of the highlighted values τ_+ and τ_- , as given in (11).

j	$s_1^{(j)}$	$\text{rate}_j^{-1}(s_1)$	$s_2^{(j)}$	$\text{rate}_j^{-1}(s_2)$	$s_3^{(j)}$	$\text{rate}_j^{-1}(s_3)$
10	0.491794333165	1.666	0.124199	-1.593	-3.7	-0.17
15	0.486321203980	1.639	0.130891	-1.461	-3.5	2.38
20	0.485861368123	1.630	0.130224	-1.596	-3.4	0.87
25	0.485821514330	1.628	0.130316	-1.483	-3.3	1.14
30	0.485818036195	1.628	0.130306	-1.569	-3.3	1.06
	0.4858177030	1.628	0.130307	-1.532	-3.1	1.08

Table 1: For each j we report the coefficients $s_i^{(j)}$, $i = 1, 2, 3$, for $k_j(-1)$, and their numerical rates of convergence as $j \rightarrow \infty$. The last row displays the 30th element of Aitken's sequence.

- The results suggest that $s_1^{(j)}$ converges to $k_G/2$ with ratio δ , that $s_2^{(j)}$ converges to $0.130307\dots$ at rate that seems to be $\alpha^2/\beta \approx (-1.532)^{-1}$; and $s_3^{(j)}$ converges to $-\pi^2 k_G/3$ at rate $\alpha^3/\beta \approx (1.082878)^{-1}$. Since this last is very close to 1 the convergence is very slow, and one should go further in j to get values of $s_3^{(j)}$ closer to the expected limit.
- The same computations for $\tau = -2$ and 0 instead of -1 show similar results.

On the other hand, concerning the sequences $\{k_j(\tau)\}_j$ we note that:

- Our numerics support that $\{k_j(\tau)\}_j$, for $\tau = -2, -1, 0$, converges to k_G at rate $1/\delta$. This agrees with the numerical results in [19] for $\tau = -2$. This rate of convergence is too slow to compute k_G with high precision. A faster alternative sequence will be chosen in Section 4.2.
- For different ranges of τ the sequence $\{k_j(\tau)\}_j$ appears to be either eventually increasing or decreasing or alternating. In Fig. 4, left and right, we have added two vertical lines that separate the regions where we can see different behaviour.
- In Fig. 4 right, $\tilde{k}_j(\tau) = \log_\delta(k_j(\tau) - k_G)$, for $j = 4, \dots, 17$. We see that

1. For $\tau \in [-2, \tau_-) \cup (\tau_+, 2)$ the graphs for different j seem to be vertically equispaced by 1 unit, that is, the rate of convergence of the sequence $\{k_j(\tau)\}_j$ seems to be $1/\delta$.
2. For $\tau \in [\tau_-, \tau_+]$ the sequence $\{k_j(\tau)\}_j$ seems to alternate around k_G and becomes eventually monotone, but this requires further detailed numerical investigations.

4.2 Obtaining an accurate approximation of Greene's constant

The computations of the sequences $\{k_j(\tau)\}_j$ lead to a method to approximate k_G . The graphs $k_j(\tau)$ are strictly decreasing functions of τ and intersect each other as shown in Fig. 4 left. For $1 \leq j < l$ let $\tau_{j,l}$ be the value of the trace such that $k_j(\tau_{j,l}) = k_l(\tau_{j,l})$. In particular, one has, computed with 50 correct decimal digits,

$$\begin{aligned}\tau_- = \tau_{3,4} &= 0.836316630998899379064771402918493203122884569070177\dots & (11) \\ \tau_+ = \tau_{2,3} &= 1.224105134257633758347076577736673021132619783370115\dots\end{aligned}$$

The basic idea to approximate k_G is based on the following numerically supported properties concerning the convergence of the sequences $\{k_j(\tau)\}_j$.

Conjecture 2. *For all $\tau \in [-2, 2)$, the sequence $\{k_j(\tau)\}_j$ converges to k_G geometrically. For $\tau = \tau^*$ (given in (6)) the rate of convergence is δ' , and $1/\delta$ otherwise. Furthermore,*

1. If $\tau \in [-2, \tau_-)$ the sequence $\{k_j(\tau)\}_j$ is strictly decreasing,
2. If $\tau \in (\tau_+, 2)$ the sequence $\{k_j(\tau)\}_j$ is strictly increasing,
3. For $\tau \in [\tau_-, \tau_+] \setminus \{\tau^*\}$, if $\tau < \tau^*$ the sequence $\{k_j(\tau)\}_j$ is eventually decreasing and, if $\tau > \tau^*$, it is eventually increasing.
4. For $\tau = \tau^*$ the sequence $\{k_j(\tau)\}_j$ alternates around k_G . Moreover the sequence of pairs of points

$$\{(\tau_{j-1,j}, k_j(\tau_{j-1,j})), (\tau_{j,j+1}, k_{j+1}(\tau_{j,j+1}))\}_j,$$

defines domains around the limit point (τ^*, k_G) that scale as δ' in τ and as δ'/δ in k .

Recall from Sect. 2.2 that the critical fixed point R_C is a map where all approximating elliptic orbits have $\text{tr}_j = \tau^*$, so as we approach R_C from the upper branch of $W^u(R_C)$ all the values of these traces accumulate to the limit value at the same rate $1/\delta$. The standard map M_k inherits this behaviour, that is, the dynamics of M_k in a length 1 interval in $\tilde{k} = \log_\delta(k - k_G)$ for values of k larger but close enough to k_G resembles the dynamics of the (one-parameter family of) maps in a fundamental domain of $W^u(R_C)$.

Further, note that the study of the sequences

$$\{\tau_{j-1,j}\}_{j \geq 2} \xrightarrow{\delta'} \tau^* \quad \text{and} \quad \{k_j(\tau_{j-1,j})\}_{j \geq 2} \xrightarrow{\delta'/\delta} k_G \quad (12)$$

does not rely on the knowledge of either of the limits. In fact, the right limit in (12) converges faster than the sequence $\{k_j(\tau)\}_j$ for fixed τ .

In [19, 17] it was already suggested to use the sequence $\{k_j(\tau^*)\}_j$ to approximate k_G , since it has rate of convergence δ'/δ , but in practice this sequence depends on the approximation of τ^* . Instead we use the sequences (12) to approximate k_G while refining the value of τ^* at the same time. We computed the pairs $(\tau_{j,j+1}, k_{j+1}(\tau_{j,j+1}))$ for $1 \leq j \leq 35$. We performed computations

with 50 decimal digits arithmetics. Using the Aitken's acceleration method we get the first 21 digits of k_G and the first 12 digits of τ^* , that is, we obtain the approximations

$$\tau^* = 0.999644540920\dots \quad \text{and} \quad k_G = 0.971635406047502179389\dots \quad (13)$$

and the estimates of the rates of convergence of sequences (12) are -0.610830 and -0.3752144 respectively.

The routines for computing the periodic orbits and get the previous results were implemented in Pari/GP [2], which allows to easily increase the precision. The code takes advantage of the symmetry lines of the standard map M_k and solves the corresponding one dimensional equation by combining bisection and Newton methods to get the desired accuracy.

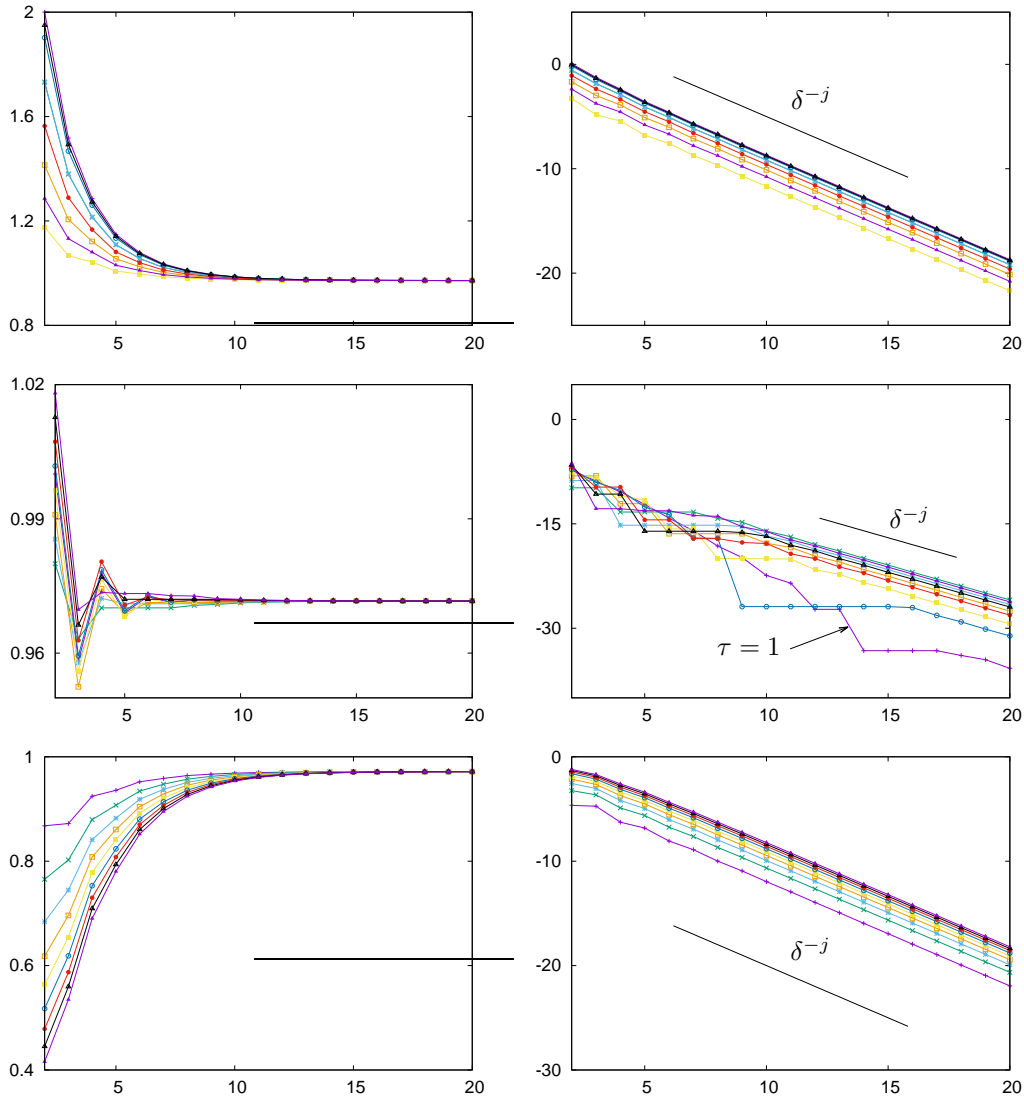


Figure 5: Left column: $k_j(\tau)$ as a function of j . Right column: $\tilde{k}_j(\tau) = \log_\delta(k_j(\tau) - k_G) + \log_\delta(2\pi)$. The values of the trace are $\tau = 2 \cos(2\pi p/q)$. Top: $p/q = 1/2, 1/3, 2/3, 1/4, 1/5, 2/5, 2/7, 2/9$, all of them give $\tau \in [-2, \tau_-)$. Middle: $p/q = 1/6$ and $p/q = p/1000$ with $163 \leq p \leq 170$, that give $\tau \in (\tau_-, \tau_+)$. Bottom: $p/q = 1/q$ for $7 \leq q \leq 15$, that give $\tau \in (\tau_+, 2]$.

Let us give some numerical evidences to support Conjecture 2 on which the previous computations are based. The left column of Fig. 5 corresponds to $k_j(\tau)$ and the right column to $\tilde{k}_j(\tau)$,

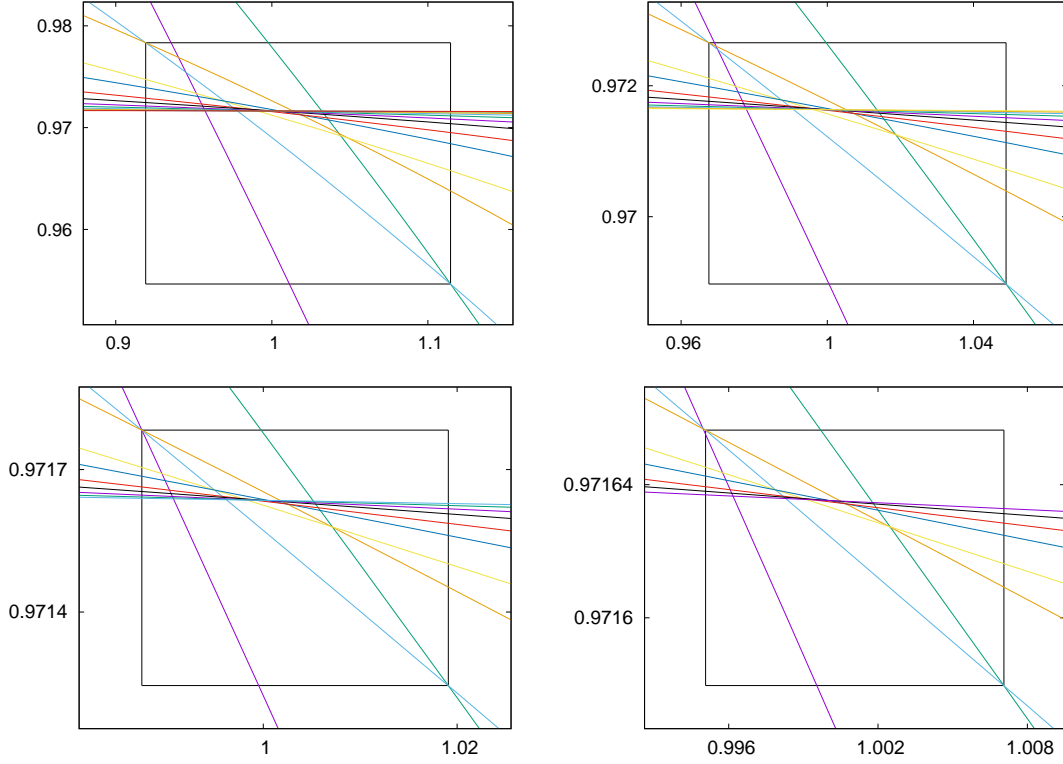


Figure 6: Magnifications of Fig. 4, left, $2\pi k_j(\tau)$ for different values of j . The upper left and lower right vertices of the inner box are of the form $(\tau_{n,n+1}, 2\pi k_n(\tau_{n,n+1}))$ and $(\tau_{n-1,n}, 2\pi k_n(\tau_{n-1,n}))$. The corresponding n and the j 's shown in each figure are: Top left: $n = 5, j = 3, \dots, 17$. Top right: $n = 7, j = 5, \dots, 17$. Bottom left: $n = 9, j = 7, \dots, 17$. Bottom right: $n = 11, j = 7, \dots, 17$.

for fixed τ as a function of j . On top, middle and bottom we show examples of $\tau \in [-2, \tau_-)$, $\tau \in (\tau_-, \tau_+)$ and $\tau \in (\tau_+, 2)$, respectively (see the caption in Fig. 5 for the actual values of τ shown). On the left we clearly see the decreasing, alternating and increasing character of the sequences predicted in Conj. 2. On the right we show $\log_\delta(k_j(\tau) - k_G)$ also as a function of j , where we added a segment with slope -1 corresponding to δ^{-j} , to stress out the fact that the rate of convergence of all the sequences shown is $1/\delta$. In the middle right plot we highlighted the behaviour of the case $\tau = 2 \cos(\pi/3) = 1$, the 1:6 resonance. Since this value of τ is very close to τ^* we checked that the sequence is monotonically increasing once $j \geq 19$.

Moreover, in Fig. 6 we show convenient magnifications of Fig. 4 left where the domains of item 4. of the Conjecture 2 can be seen. The fact that these domains present these scalings may be useful to eventually derive a limit approximation of the dynamics of these islands of stability.

Remark 4.1. Greene's criterion deals with the behaviour of the traces tr_j as a function of k . Indeed, if in Fig. 4 one considers the sequence of intersections of the horizontal line $\{k = k^*\}$ with the graphs of $k_j(\tau)$, one observes the behaviour supported by Greene's conjecture, that is,

1. if $k^* < k_G$, the sequence $\{\text{tr}_j(k^*)\}_j$ is bounded and tends to 2 (sub-critical case),
2. if $k^* = k_G$, the sequence $\{\text{tr}_j(k^*)\}_j$ is bounded and tends to τ^* (critical case),
3. if $k^* > k_G$, the sequence $\{\text{tr}_j(k^*)\}_j$ tends to $-\infty$ (super-critical case).

We emphasize that in the sub-critical case there is an analytic RIC, see [8, 18].

4.3 The size of the approximating islands and the flux through them

In this section we investigate the behaviour of the following two observables as the order j of the approximants increases:

1. The size μ_j of the stability domain DS_j around the j approximant elliptic (or reflexive hyperbolic) periodic orbit.
2. The so-called Mather's ΔW_j [24] which is commonly used to describe transport properties of twist maps. Recall that Mather's ΔW can be seen as the flux, that is, the area per iterate that crosses a turnstile, see [21]. By ΔW_j we refer to the flux through the j th approximating pair of periodic orbits.

Let us briefly recall the concepts of flux and turnstile mentioned above. Given a region with a piecewise smooth boundary, the flux is the volume of the subset of points of the region that escapes from the region at each iterate. Then, for a twist map of the cylinder, to define the flux through a pair of Birkhoff periodic orbits of the same rotation number, one considers a simple closed rotational curve C joining the successive points on the pair of hyperbolic and elliptic (or reflexion hyperbolic) periodic orbits and such that the intersection of the curve C with its image reduces to the points on the pair of approximating orbits. Then the flux through the pair of periodic orbits is given by the flux through the region delimited by C (upper or lower region in the cylinder). Note that the curve C and its image define exit and incoming sets to the region, hence it acts as a turnstile. We refer to [26] for a review of these concepts.

4.3.1 Behaviour of μ_j and ΔW_j as a function of τ .

Let us consider a fixed value of τ and recall that, for each approximant j , $k_j(\tau)$ denotes the value of the parameter k for which the j -approximating elliptic (or reflection-hyperbolic) periodic orbit has trace equal to τ . Denote by DS_j the stability domain around such orbit. We aim to investigate the measure of DS_j and discuss how it behaves as j increases.

Numerical evidences support that the standard family of maps is close to $W^u(R_C)$, where R_C is the critical fixed point of the renormalisation operator \mathcal{R}_1 . Hence, in particular, we expect the stability domains DS_j of the approximating islands to scale as $(\alpha\beta)^{-j}$ for the j th approximant, provided j is large enough, see (4)-(5). Indeed, for different j , we compare the sizes μ_j of DS_j scaled according to (8). The numerical approximation of μ_j is obtained as follows.

1. We consider $\tau \in [-4.5, 2)$. For $\tau < -4.5$ the islands are not detected with the resolution used in computations. For each of the values of τ considered we obtain $k_j(\tau)$.
2. To approximate μ_j we consider a 800×800 equispaced grid in $(\xi, \eta) \in [-1, 1] \times [-0.6, 0.6]$. Each point of the grid defines a point in the original coordinates (x, y) which is considered to be in DS_j if it stays in $[-1, 1] \times [-0.6, 0.6]$ for at least 10^5 iterates. Then, using these criteria, we compute

$$\tilde{\mu}_j = \frac{\mu_j}{d_x^{(j)} d_y^{(j)}}, \quad \text{with} \quad \mu_j \approx \frac{\#DS_j}{64 \cdot 10^4},$$

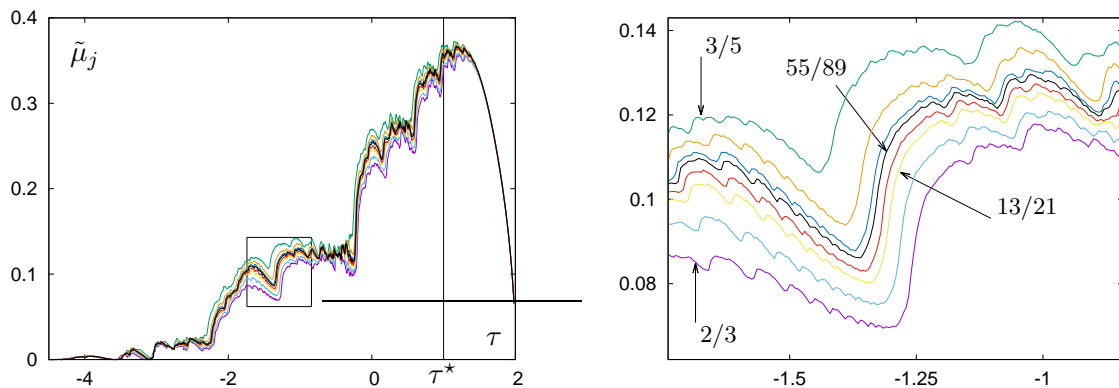


Figure 7: Left: $\tilde{\mu}_j$ as a function of τ for $j = 2, \dots, 9$ (that is, for periodic orbits with rotation number from $1/2$ to $55/89$). The vertical line corresponds to the limit value of the trace τ^* . Right: Magnification of the left plot.

where $\#DS_j$ denotes the number of points of the grid that are considered to be in DS_j .

Note that μ_j includes both regular and confined chaotic orbits in the island. On the other hand, an orbit that we consider to be confined actually remains stuck close to the whole island chain of the standard map for at least $10^5 \times q_j$ iterates.

Computations were performed for $2 \leq j \leq 9$ (up to rotation number $55/89$) and taking a fine grid of values of $\tau \in [-4.5, 2)$. In Fig. 7 we show the evolution of $\tilde{\mu}_j$ as a function of the trace τ . The right plot is a magnification of the left one. We observe that the curves $\tilde{\mu}_j(\tau)$ alternate as j increases around a “limit curve” which would correspond to the evolution of the size of the stability domain of the “limit” islands when $j \rightarrow \infty$.

Next, let us consider Mather’s ΔW_j along the sequence of best approximants of the golden number. Since ΔW_j is the area per iterate that crosses a turnstile [21] it can be approximated by the number of pixels of a grid with $\eta > 0$ and that M^q maps to points with $\eta < 0$. In the computations we used the same grid as before for estimating μ_j . From the set of points that cross $\eta = 0$ we also check if those can be considered to be ‘confined in an island’. As before, a point is considered ‘confined in an island’ if remains stuck close to the island chain for at least $10^5 \times q_j$ iterates. Hence, following this criterion, we express

$$\Delta W_j = \Delta W_j^c + \Delta W_j^{nc},$$

where the superscript c stands for ‘confined in an island’ and nc for ‘non-confined in an island’. To compare the values of ΔW_j for different j we take into account the scalings in (8), that is, we compute

$$\Delta \tilde{W}_j = \frac{\Delta W_j}{d_x^{(j)} d_y^{(j)}}$$

In Fig. 8 we show, from left to right, $\Delta \tilde{W}_j$, $\Delta \tilde{W}_j^{nc}$ and $\Delta \tilde{W}_j^c$, respectively, as a function of τ . We have used the same grid used to approximate $\tilde{\mu}_j$ in Section 4.3. Comparing the left and center plots we see that most of the turnstile area is in $\Delta \tilde{W}_j^{nc}$, but there is still some part of the island that is included in $\Delta \tilde{W}_j$. Compare the right plot in Fig. 8 with the left plot in Fig. 7.

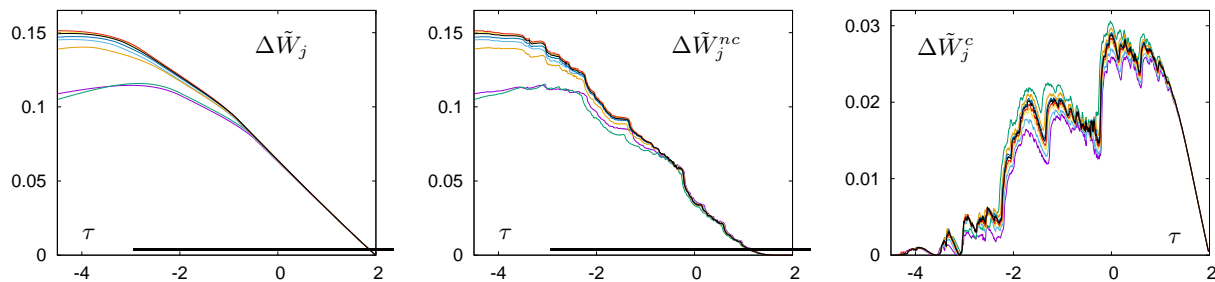


Figure 8: $\Delta\tilde{W}_j$ (left), $\Delta\tilde{W}_j^{nc}$ (center) and $\Delta\tilde{W}_j^c$ (right), as a function of $\tau \in (-4.5, 2)$. The curves correspond to the same rotation numbers as shown in Fig. 7. Note that the order of the curves corresponding to different rotation numbers changes, the color identifies each curve in each plot.

4.3.2 Behaviour of μ_j and ΔW_j as a function of $k > k_G$.

To study escape rates across the golden Cantorus we look for the area of the stability domain of the approximating islands for $k > k_G$. In Subsect. 4.1 we saw that if $\tau < \tau_-$, then the sequence $\{k_j(\tau)\}_j$ converges monotonically and geometrically to k_G with ratio δ . In Fig. 9 we show $\tilde{\mu}_j$ as a function of $\tilde{k} = \log_\delta(k - k_G) < 0$. As in Fig. 7 we used a 800×800 equispaced grid in $(\xi, \eta) \in [-1, 1] \times [-0.6, 0.6]$, and considered that a point in this region is non-escaping (and hence belongs to DS_j) if it remains in this box for, at least 10^5 iterations of the map $\Lambda_j^{-1} \circ M_k^{q_j} \circ \Lambda_j$. The results in Fig. 9 show $\tilde{\mu}_j(\tilde{k})$ for $j = 3$ (period 2/3) to $j = 13$ (period 233/377) in the range $\tilde{k} \in [-12, -3]$, that is, for $k \in [0.974521477288362, 1.20341583474535]$. The 14th approximating periodic orbit corresponding to rotation number 377/610 has no detectable area (with the resolution used) surrounding it in the range of \tilde{k} shown.

We observe in Fig. 9 that, as j increases, the shape of the curves roughly seems to get closer to a limit shape, that is, $\lim_{j \rightarrow \infty} |\tilde{\mu}_j(\tilde{k} + 1) - \tilde{\mu}_{j+1}(\tilde{k})| = 0$, and $\lim_{\tilde{k} \rightarrow -\infty} \tilde{\mu}_j(\tilde{k}) = \tilde{\mu}_j(k_G)$. Nevertheless, on top left of Fig. 9 we can see that for each j , $\tilde{\mu}_j(\tilde{k})$ seems to tend to a different limit value as $\tilde{k} \rightarrow -\infty$. This is consistent with the results in Fig. 7, where we saw that the scaled areas of consecutive approximants alternate around the limit.

Let us also report the results about ΔW . Similar to Fig. 8, we plot the corresponding total, non-confined and confined turnstile areas of the islands shown in Fig. 9 and in Fig. 10. These turnstile areas are those that actually play a role in transport properties, see related comments in Section 5.

Finally, let us illustrate the stability islands in Fig. 11 for a length 1 interval of \tilde{k} , $\tilde{k} = [-10, -9]$. We plot the islands of rotation number 13/21 up to the ones with rotation number 89/144 (a total of 5 approximants) for $\tilde{k} = -9.125(-0.125) - 10.000$. We see that the island with rotation number 13/21 (rightmost column) does not change much in this interval of \tilde{k} , while the islands with larger period change at a faster rate. Even the last one shown (that with rotation number 89/144) disappears in this range of \tilde{k} . The scaled area that these islands occupy can be seen in Fig. 9. Each row in Fig. 11 corresponds to a fixed value of \tilde{k} .

In Fig. 9 we can see sudden decreases in the scaled confined area. From the displayed evolutions in Fig. 11 we can guess to which satellite islands these correspond to. Recall that the sudden decreases in the confined area are related to the breakdown of an invariant curve that allows

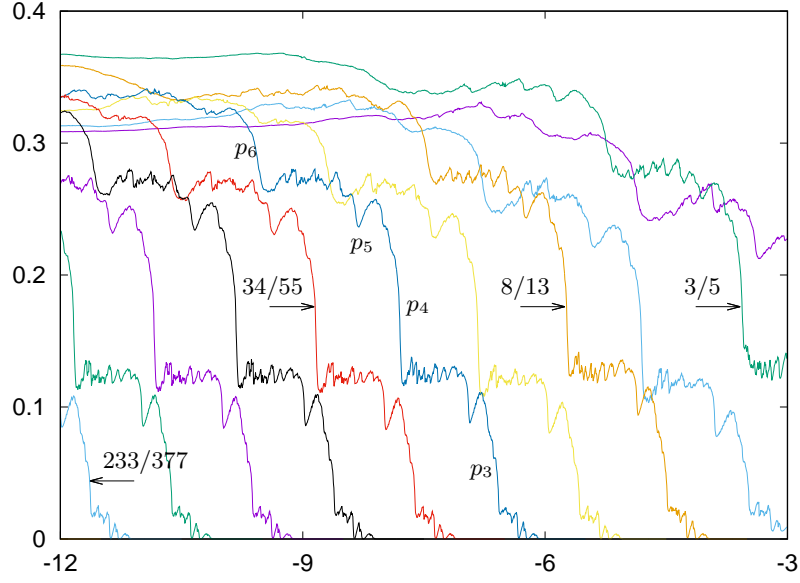


Figure 9: Scaled areas of approximating islands $\tilde{\mu}_j(\tilde{k})$, where $\tilde{k} = \log_\delta(k - k_G)$ for $j = 3, \dots, 13$. Some of the curves are labelled with the rotation number they correspond to. This figure is related to Fig 7. Here \tilde{k} is used as parameter instead of τ , and only the data on the left of τ^* in Fig 7, left, is shown. See text for further explanations.

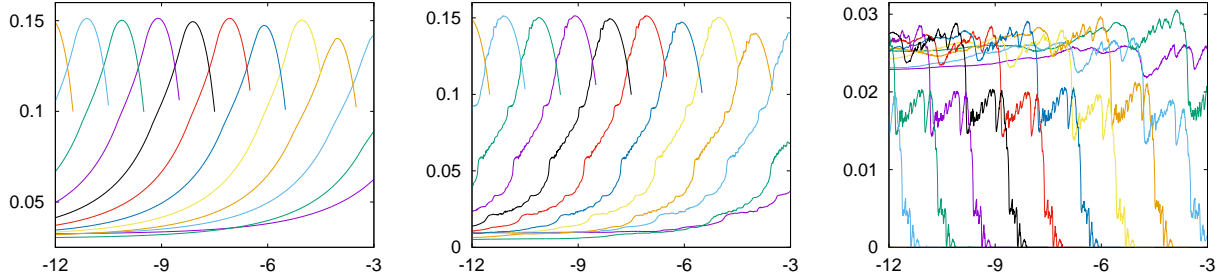


Figure 10: We display $\Delta\tilde{W}_j$ (left), $\Delta\tilde{W}_j^{nc}$ (center) and $\Delta\tilde{W}_j^c$ (right) as a function of \tilde{k} . The left and center plots display the curves for $3 \leq j \leq 14$ but the curve for $j = 14$ is not shown in the right plot.

previously chaotic confined region to escape from a compact set that contains the whole island, see for example [29, 30]. At this global bifurcation satellite islands leave the connected component of the domain of stability. We labelled some of the jumps in Fig. 9 as p_3 , p_4 , p_5 and p_6 to refer to the effect of the breakdown of the invariant curves surrounding the islands of rotation number $1/3$, $1/4$, $1/5$ and $1/6$, respectively.

5 Transport across a golden Cantorus

The gaps of a Cantorus allow orbits to leak across it, but the time to cross them can be very large, specially for parameters just after the breakdown. In this section we study escape rates

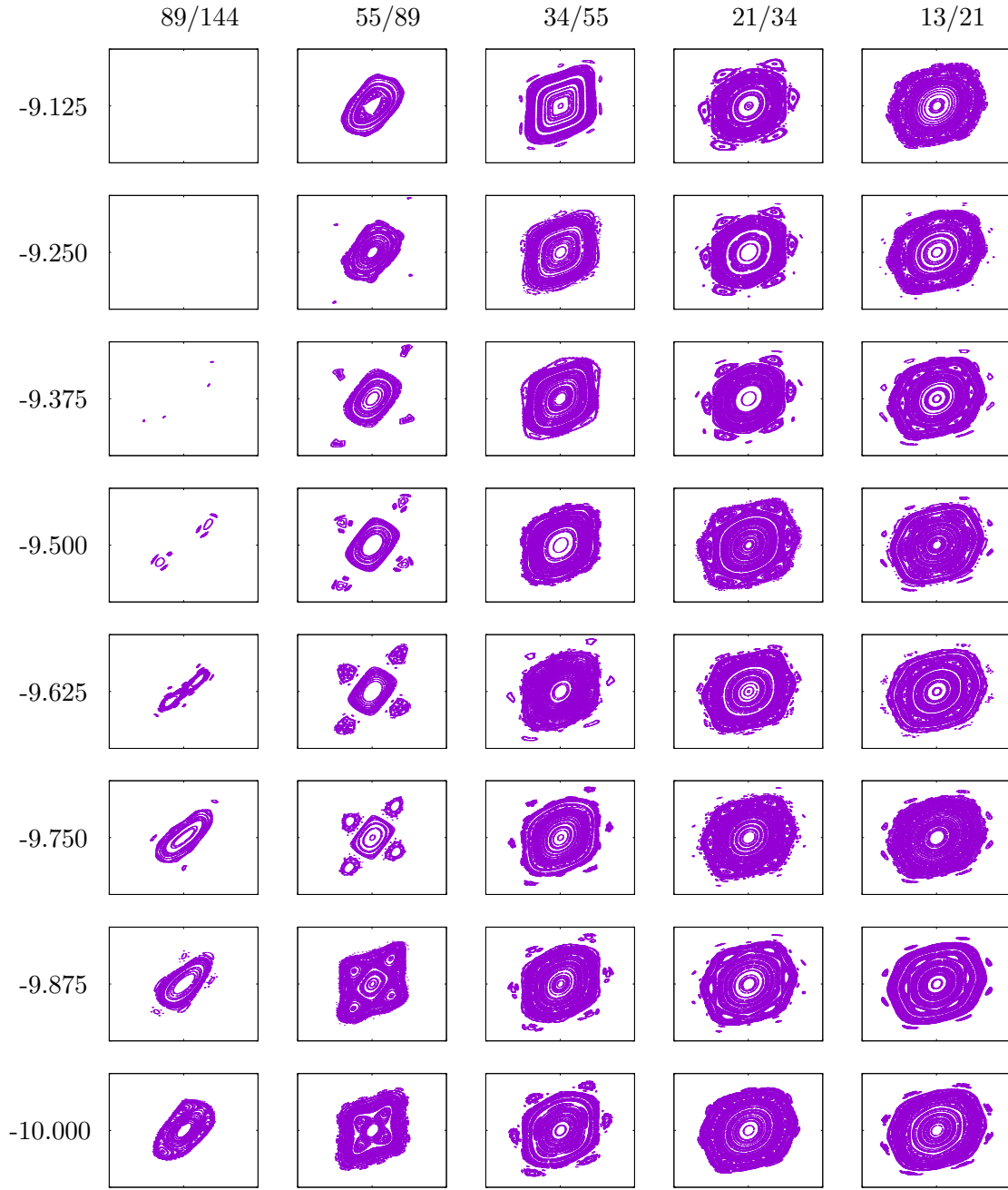


Figure 11: Evolution of the shape of approximating islands with rotation numbers $13/21, 21/34, 34/55, 55/89$ and $89/144$ in the interval $\tilde{k} \in [-10, -9)$. We show the shape of these islands for the eight values $\tilde{k} = -9.125(-0.125) - 10.000$. See text for further explanations.

across the golden Cantorus of the standard map M_k for $k > k_G$ but close to k_G . First, we study the behaviour of the mean escape rate and its standard deviation as $k \rightarrow k_G$. Next, we consider the stopping time of the previous escape process and look for its probability distribution.

5.1 Escape rates

For $k < k_G$, but close to k_G , the standard map M_k has a RIC with rotation number ω , the golden mean, and another RIC with rotation number $1 - \omega$, which is symmetric of the previous one with respect to the point $(1/2, 1/2)$. These curves intersect the y axis in points close to $(0, y^*)$ and $(0, 1 - y^*)$, respectively, where $y^* \approx 0.664759$ (this value y^* is not the minimum, which is close to 0.5296, nor the maximum, which is close to 0.6848, of the RIC with rotation number ω). But these RIC have points with $y > y^*$ and $y < 1 - y^*$, respectively.

We can take initial conditions in the chaotic region between these curves to see how many iterates are needed to cross one of the Cantori with rotation number ω or $1 - \omega$ which replace the RIC for $k > k_G$. A simple way is to consider a set $\mathcal{U}(k)$ of initial conditions in a fundamental domain of one of the branches of the local invariant unstable manifold, $W_{H_2}^u$, of the period 2 saddle orbit of M_k , which for $k < k_G$ is located between the two invariant RIC.

Concretely, if we consider the formulation of the standard map with $x, y \in [0, 2\pi)$ to obtain H_2 we look for an initial point $x \in [0, \pi/2)$ with $y = 2x$ and such that the image is the symmetric point $(2\pi - x, 2\pi - 2x)$. The image of this second point is the first one. This implies that x has to be a solution of the equation $4x + k \sin(x) = 2\pi$, which has a unique solution in $(0, \pi/2)$ for all $k > 0$. Concretely, for values of k until approximately 1 the solution is close to $\pi/2 - k/4$. For k large it tends to behave as $2\pi/(k + 4)$.

Because of the symmetry it is immediate to check that the differential map is the same in both points. The dominant eigenvalue of the differential at the first point, say γ , behaves as $1 + k/2$ for k small, it is ≈ 1.624863 for $k = 1$ and approaches $k + 2$ for k large. Hence, the dominant eigenvalue of the differential of the period 2 orbit H_2 is γ^2 .

Given $(x_0, y_0) \in \mathbb{S}^1 \times (0, 1)$ denote by $(x_n, y_n) = M_k^n(x_0, y_0) = M_k(x_{n-1}, y_{n-1})$. Let $n = n(x_0, y_0)$ be the number of iterates for which either $y_n > y^{(u)}$ or $y_n < y^{(l)}$ for the first time, where $y^{(u)}$ and $y^{(l)}$ denote upper and lower limits. We shall take $y^{(l)} = 0$ and $y^{(u)} = 1$ in the computations, but other values are possible. One can take $y^{(l)} \in (0, 0.3]$ and $y^{(u)} \in [0.7, 1)$, for instance. If $n = n(x_0, y_0) < \infty$ we say that (x_0, y_0) escapes across one of the golden Cantori in n iterates.

Taking the initial conditions in $\mathcal{U}(k)$ they are candidates to escape, hence with $n(x_0, y_0) < \infty$. For values of $\Delta k = k - k_G > 0$ small, we have numerically approximated the probability law

$$N_k(m) = P(n(x_0, y_0) = m), \quad m \in \mathbb{N}, \quad (14)$$

and we have computed its average $\langle N_k \rangle$ and its standard deviation σ_k . That is, if \mathbf{ic} is the number of initial conditions in $\mathcal{U}(k)$, then we have studied the behaviour of

$$\langle N_k \rangle = \frac{1}{\mathbf{ic}} \sum_{u \in \mathcal{U}(k)} n(u) \quad \text{and} \quad \sigma_k^2 = \frac{1}{\mathbf{ic}} \sum_{u \in \mathcal{U}(k)} (n(u))^2 - \langle N_k \rangle^2. \quad (15)$$

Concretely, we have computed the mean escaping time for 1101 values of the parameter k in an equispaced grid in \log_δ -scale. We have considered $\tilde{k} = -3(-0.01) - 14$. Since we expect the mean escaping time to behave as a negative power law in $k - k_G$, we have considered less initial conditions as we approached the breakdown value of the parameter k_G . Namely 10^4 initial conditions for $\tilde{k} = -12(-0.01) - 14$ (but for some of them in this range up to 10^5), 10^5 initial conditions for $\tilde{k} = -9(-0.01) - 11.99$, 10^6 for $\tilde{k} = -6(-0.01) - 8.99$ and 10^7 for $\tilde{k} = -3(-0.01) - 5.99$.

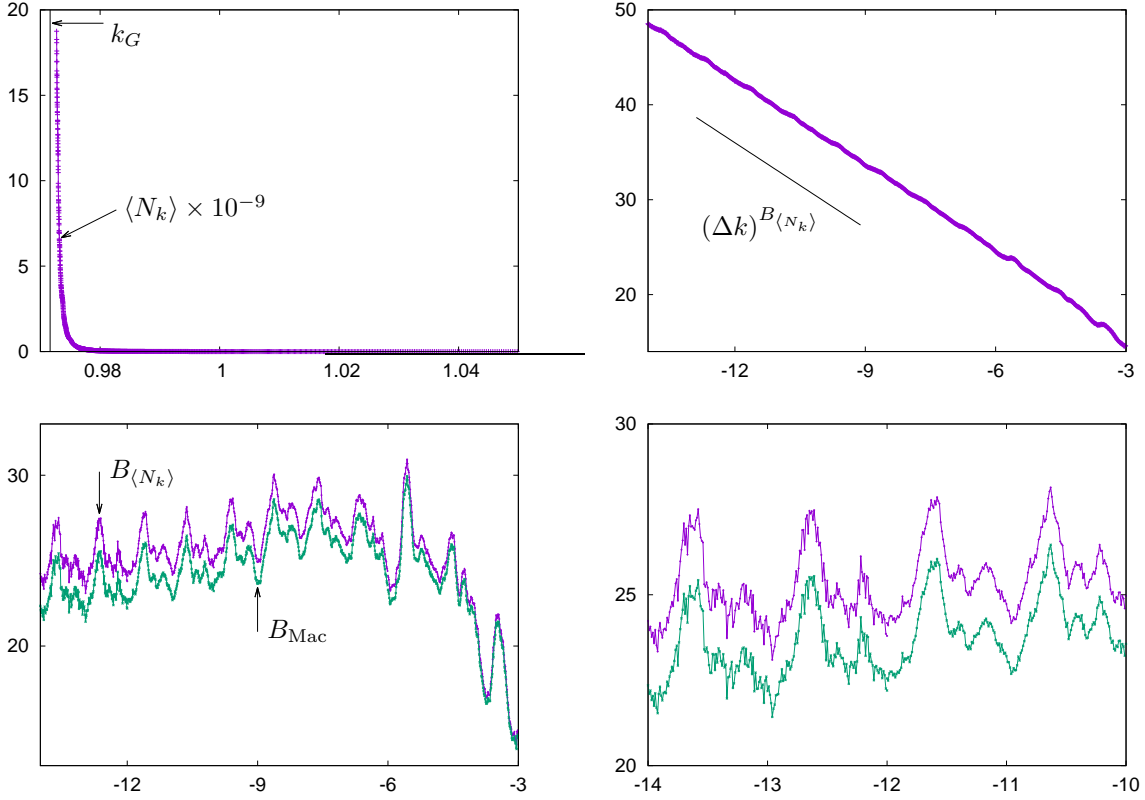


Figure 12: Statistics of $\langle N_k \rangle$, the mean escaping time of orbits of the Chirikov standard map (1), for values of the parameter near k_G . Top left: $\langle N_k \rangle \times 10^{-9}$ as a function of k (purple), $\{k = k_G\}$ (black). Top right: $\log_\delta \langle N_k \rangle$ as a function of \tilde{k} (purple), and the slope $B_{\langle N_k \rangle}$ (black). Bottom left: $\langle N_k \rangle \times (k - k_G)^{-B}$, with $B = B_{\langle N_k \rangle}$ (purple, top) and $B = B_{\text{Mac}}$ (green, bottom), as a function of \tilde{k} , see (18). Bottom right: Detail of bottom left. Compare with Fig. 9 and Fig. 10. See text for further explanations.

The evolution of the mean $\langle N_k \rangle$ as a function of k can be seen in Fig. 12. There we show the same data in different scales. First, on top left, one can see the direct results for the mean as $k \rightarrow k_G$. As expected, we observe substantial increase in the mean escaping time as we approach k_G (highlighted as a vertical line in this plot). There we show $\langle N_k \rangle \times 10^{-9}$. The value of k closest to k_G shown in Fig. 12, top left, corresponds to $k = 0.972724398546588 \approx k_G + \delta^{-14}$, being $\delta^{-14} \approx 1.089 \times 10^{-3}$. In average, for this value of k each initial condition needs over 1.5×10^{10} iterates to leave $y \in [0, 1]$.

In order to explain the bottom plots in Fig 12 let us recall that for any irrational rotational number ω , Mather's ΔW_ω is defined as the limit of $\Delta W_{p_j/q_j}$ over sequences of rationals $\{p_j/q_j\}_{j \geq 0}$ tending to ω , see [24]. On the other hand, it follows from renormalisation theory, see [17, 19], that Mather's ΔW_ω satisfies

$$\Delta W_\omega(k_G + \Delta k/\delta) \approx \Delta W_\omega(k_G + \Delta k)/(\alpha\beta),$$

so that there exists a 1-periodic universal function $U(x) = U(x + 1)$ such that

$$\Delta W_\omega(k_G + \Delta k) \approx A(\Delta k)^B U(\log_\delta(\Delta k)), \quad \text{where } B = \log_\delta(\alpha\beta). \quad (16)$$

As a consequence, we expect **the mean time to escape** $\langle N_k \rangle$ to behave as an inverse power law

Interval	B	A
$[-14, -12]$	-3.00 ± 0.01	25 ± 1
$[-14, -11]$	-2.978 ± 0.005	28 ± 1
$[-14, -10]$	-2.978 ± 0.003	28.7 ± 0.5

Table 2: Approximate constants in (17) obtained by least square fitting in different ranges.

in Δk , that is,

$$\langle N_k \rangle = A(\Delta k)^B \quad (17)$$

In Fig. 12 top right, we show $\log_\delta \langle N_{\tilde{k}} \rangle$ as a function of $\tilde{k} = \log_\delta(\Delta k)$. Note that, as $k \rightarrow k_G$, the slope seems to change slightly. A linear fit of the data in different ranges of \tilde{k} provides approximations of the constants A and B in (17), we show some results in Table 2. The slope shown as a reference in Fig. 12 top right is $B_{\langle N_k \rangle} = -3.00$, that is, the one obtained for the linear fit in the interval $\tilde{k} \in [-14, -12]$. Note that the expected theoretical value according to (16) is

$$B = B_{\text{Mac}} = -\log_\delta(\alpha\beta) \approx -3.01172189133849. \quad (18)$$

Our numerical results based on direct simulations of the standard map M_k show that $B_{\langle N_k \rangle}$ seems to approach to B_{Mac} as we approach the breakdown.

In Fig. 12 bottom, left and right, we show $\langle N_k \rangle \times (k - k_G)^{-B}$, as a function of \tilde{k} . As labelled in the bottom left figure, the top graph corresponds to choosing $B = B_{\langle N_k \rangle} = -3.00$ while the one below corresponds to $B = B_{\text{Mac}}$. The right plot is a magnification of the leftmost oscillations of the left plot. The oscillations in $\tilde{k} \in [-14, -12]$ are less smooth since we had to consider 10 times less initial conditions than in $\tilde{k} \in [-12, -10]$.

We observe in the bottom plots of Fig. 12 that, after subtracting the power-law tendency, there seems to be a 1-periodic behaviour as we approach the breakdown. This periodic behaviour is due to the 1-periodic function $U(\log_\delta(k - k_G))$ in (16). Also the fluctuations far from k_G ($\tilde{k} > -6$ in Fig. 12, bottom left) seem to be related to this 1-periodic behaviour close to k_G , but strongly deformed.

The numerical results included in this paper suggest that the shape of the 1-periodic fluctuations shown in the figure is a consequence of the shape and area of the approximating islands (see Fig. 9), the turnstile area (see Fig. 10 and compare it with Fig. 12: minima in Fig. 12 approximately correspond to maxima in Fig. 10, left and center), the area of the lobes created by the invariant manifolds of hyperbolic approximating periodic orbits, and stickiness effects due to the fine structure of the border of the stability islands.

Let us report now the results of the computations related to the standard deviation σ_k (15). In Fig. 13 we show that the standard deviation σ_k seems to behave similarly to the mean. On the left of this figure, we plot σ_k as a function of k , and on the right we plot $\log_\delta(\sigma_{\tilde{k}})$ as a function of \tilde{k} and the slope $B_{\langle N_k \rangle}$. Compare with the plots in Fig. 12 top.

Despite having a similar behaviour as $k \rightarrow k_G$, as an inverse power law in Δk with the same power that in the case of $\langle N_k \rangle$, the main difference between the two observables is the existence of peaks in σ_k , that are much more prominent far from the breakdown. Namely, as one can observe

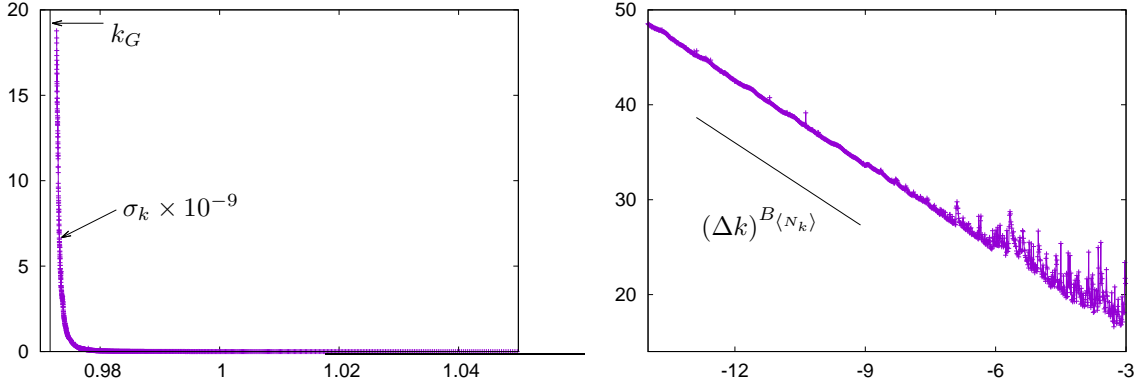


Figure 13: On the left plot we display $\sigma_k \times 10^{-9}$ as a function of k (purple), $\{k = k_G\}$ (black). The right plot shows $\log_\delta(\sigma_{\tilde{k}})$ as a function of \tilde{k} (purple), and the slope $B_{\langle N_{\tilde{k}} \rangle}$ (black).

in Fig. 13, right, despite we can see some small peaks near $\tilde{k} \approx -10$, the largest deviations from the straight line appear for $\tilde{k} > -8$. In Fig. 14 we plot $\sigma_{\tilde{k}} / \langle N_{\tilde{k}} \rangle$ as a function of \tilde{k} . On top left we see the behaviour in the whole range considered, $\tilde{k} \in [-14, -3]$, while the other figures are magnifications of this first one. These magnifications allow to see the actual shape of the peaks. In all the plots, we show a black horizontal line that corresponds to $\sigma_{\tilde{k}} / \langle N_{\tilde{k}} \rangle = 1$. It is remarkable that besides the peaks, the statistics of escape rates seem to have close values of the mean and the standard deviation.

So far, we have presented the results of a massive evaluation of the mean escaping time across the golden Cantorus of the standard map. The following remarks on the obtained results could help to interpret them correctly:

1. The power law behaviour $\langle N_{\tilde{k}} \rangle \sim (\Delta k)^{-B_{\text{Mac}}}$. In our simulations we approached the breakdown by $\delta^{-14} \approx 0.00108$ and got a difference between the theoretical value and our experimental approximation $|B_{\text{Mac}} - B_{\langle N_{\tilde{k}} \rangle}| = \mathcal{O}(10^{-2})$. This means that we are still far from the limit, but computing representative statistics for values of \tilde{k} smaller than -14 is still far from practical. Note further that if we were close enough to the limit, the oscillations in Fig. 12 should take place around a horizontal line. But we expect this to happen closer to the limit, that is, as $\tilde{k} \rightarrow -\infty$.
2. The visible peaks in $\sigma_{\tilde{k}} / \langle N_{\tilde{k}} \rangle$ and the stickiness effect of islands of stability. We see in Fig. 14 that, for values of $\tilde{k} < -8$, there is little effect due to the stickiness of stability islands, if any. This is mainly due to the fact that the time to cross the Cantorus is of an order of magnitude larger than the mean trapping time around any of the islands that are present in the phase space.

On the other hand, in the figure we see that there are many visible peaks, that seem to be more prominent for $\tilde{k} > -8$. Recall that the way initial conditions are chosen ensures that all of them will eventually escape. Hence σ_k remains bounded in any case, but it is expected to strongly depend on the number of initial conditions, $\sigma_k = \sigma_k(\text{ic})$. In Fig. 15 we show examples of this strong dependence: we plot $\sigma_{\tilde{k}}(\text{ic})$ for $\tilde{k} \in [-5, -3]$ and $\text{ic} = 10^5, 5 \times 10^5, 10^6, 5 \times 10^6$ and 10^7 . Note that the values of $\sigma_{\tilde{k}}(\text{ic})$ do not increase as ic does. Here, the initial conditions of the case $\text{ic} = 5 \times 10^5$ are those of $\text{ic} = 10^5$ plus 4×10^5 extra initial conditions, and so on.

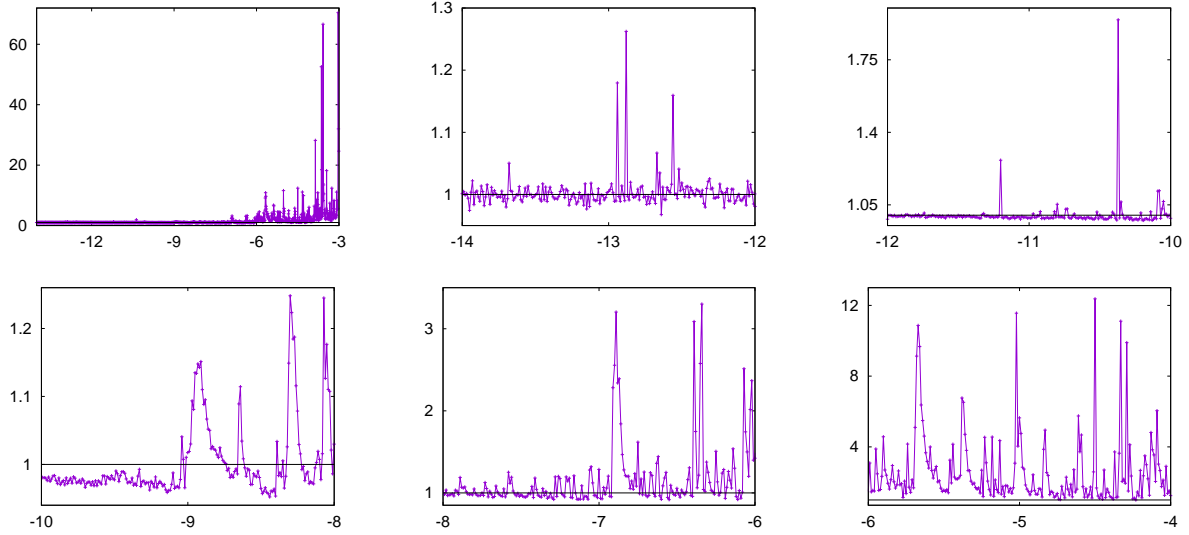


Figure 14: Top left: $\sigma_{\tilde{k}} / \langle N_{\tilde{k}} \rangle$ as a function of \tilde{k} in $\tilde{k} \in [-14, -3]$. The other plots are magnifications in: top middle: $[-14, -12]$, top right: $[-12, -10]$, bottom left: $[-10, -8]$, bottom middle: $[-8, -6]$ and bottom right: $[-6, -4]$.

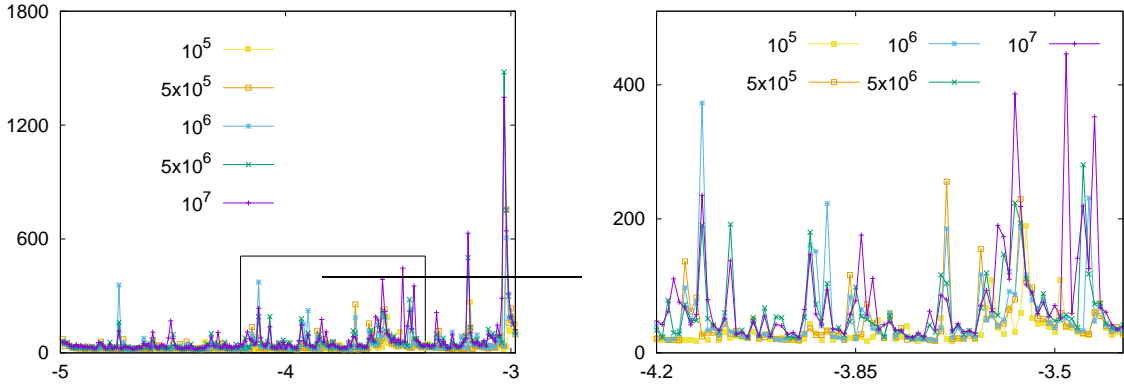


Figure 15: Left: $\sigma_{\tilde{k}} \times (k - k_G)^{B_{\text{Mac}}}$ as a function of $\tilde{k} \in [-5, -3]$, obtained for different values of B_{Mac} , see the key in the plots. Right: Magnification of the domain marked in the left plot.

3. The limit 1-periodic oscillations $U(\log_{\delta}(k - k_G))$. The power-law behaviour comes from the scaling in area and in parameter, but yet it needs to be clarified which are the objects responsible for the actual transport probabilities. One expects the oscillations to be strongly related to the area of the heteroclinic lobes of intersecting invariant manifolds of hyperbolic periodic orbits and the turnstile areas of approximating orbits. Namely, as k varies, the area in the phase space that is accessible to orbits that can escape changes as the islands of stability do, and not in a monotone way in \tilde{k} , but if we conveniently scale the phase space, the area occupied by evolving islands varies in a periodic way, recall Sect. 4.3, and also Figs. 9 and 10.

We end up this section by referring to previous works where similar simulations were performed:

- To our knowledge, the first similar computations were done in [5], where a total number

of 100 orbits starting at $\{y = 0\}$ were iterated under M_k for (at most) 10^7 times, keeping track on the number of iterates needed to eventually cross the line $\{y = 0.5\}$. As a result of the computations, a fit of the power law (17) provided the coefficients $A = 103$ and $B = 2.55$. However, values of k in $(k_G, 2\pi)$ were used in the computations. In particular, for the largest values for which the statistics are computed, there are almost no visible stability islands in the phase space and the diffusion coefficient $D(k)$ grows as k^2 , see [27]. This might be the reason why the value of A is much larger than the value we obtain.

- The power law behaviour was theoretically justified in [21]. In this work, the authors fixed $B = B_{\text{Mac}}$ as theoretical value and the value of $A \approx 25$ in (17) was obtained. These values are close to the ones we obtain, see Table 2.
- Finally, in [7] the authors give numerical evidence of the predictions from renormalisation theory [19, 17] and transport theory [21]. They computed the diffusion coefficient averaged among 5000 initial conditions. They restricted themselves to $1 \leq k \leq 2.5$, and in this range they were able to get satisfactory results for the exponent B in (17). In the whole range, they got $B = 3.24$. In $1 \leq k \leq 1.4$ they got $B = 3.16$ and in $1.4 \leq k \leq 2.5$ numerical simulations gave $B = 2.96$, which is closer both to the theoretical result B_{MMP} obtained in [21] and to the value we obtain. The value of the constant A in (17) was not reported.

As a final comment, we want to note that the computation of escape rates near Greene’s critical values is still a hard computational issue. To obtain the results shown in Figures 12 and 13 we had to perform over 8.33×10^{15} iterations of the standard map (1). The sharpness of the above results in the literature is still remarkable.

5.2 The probability law of escape rates

In this subsection we approximate the probability density function (pdf) of N_k (14). To this end, we compute histograms with bins of constant length for integer values of $\tilde{k} \leq -5$ as follows. Let $T = [t_0, t_1]$ a time interval, depending on k , for which most initial conditions (chosen as in the previous section) escape in a number of iterations that is contained in T . Then we consider n_i sub-intervals $I_j = [t_0\lambda^j, t_0\lambda^{j+1})$, where $\lambda = (t_1/t_0)^{1/n_i}$, and a counter C_j initially set to 0, $j = 0, \dots, n_i - 1$. Each initial condition adds a unit to C_j if escapes in m iterates, where $m \in I_j$. To recover the pdf from the histogram we divide each counter by the length of the interval and by the total number of initial conditions, **ic**, that is, we plot $C_j/((n_i + 1)\text{ic})$.

We show the pdf’s obtained in Fig. 16. On the left we can see the pdf N_k in the actual scale time for $\tilde{k} = -5(-0.5) - 12$, and on the right we display these same pdf’s, but in decimal logarithmic scale in time, that is, we plot

$$N'_k(\xi) = \log(10)10^\xi N_k(10^\xi). \quad (19)$$

The pdf’s were computed using $n_i = 400$, $t_0 = 10^3$ and $t_1 = 10^9$ for $\tilde{k} \geq -10$ while $t_1 = 10^{11}$ otherwise. We have labelled some pdf’s according to the value of \tilde{k} they correspond to. In both plots, left and right, one can follow N_k for decreasing values of \tilde{k} by following the maximum of each pdf from left to right. In the left plot, one observes that the pdf’s accumulate to 0 as k goes further apart from k_G . To see what happens for $k \rightarrow k_G$, the right plot is more convenient. The pdf’s in \log_{10} -scale in the number of iterates appear to be equispaced since they correspond to equispaced values of \tilde{k} and $\langle N_k \rangle \sim (\Delta k)^B$. Note that, in \log_{10} scale for the number of iterates, the pdf’s evolve from a seemingly symmetric shape to some asymmetric shape as \tilde{k} decreases.

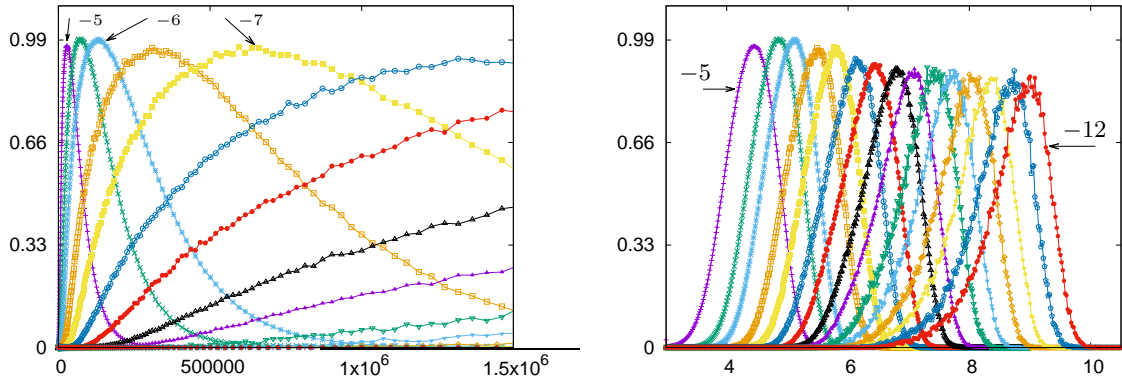


Figure 16: Estimates of the probability density function (pdf) of the number of iterates needed to escape, N_k , for different values of \tilde{k} . Left: N_k in the original scale of time. Right: N'_k vs ξ , see (19). Here we show the pdf's for $\tilde{k} = -5.0(-0.5) - 12.0$.

Concerning the underlying probability law, a Kolmogorov-Smirnov test of adjustment was performed to see if the experimental data followed the hypothetical gamma pdf with the adjusted parameters. We recall that the gamma pdf $G(x; \kappa, \theta) = x^{\kappa-1}e^{-x/\theta}/(\Gamma(\kappa)\theta^\kappa)$ is defined for $x > 0$ and depends on the shape and scale parameters $\kappa, \theta > 0$. We tried a gamma pdf because of the apparent similitude between the gamma pdf and the plots in Fig. 16 left. In all cases studied, the statistic D (the largest vertical distance between the experimental cumulative distribution function (cdf) and the cdf of the theoretical distribution) was $D \approx 0.02$. Unfortunately, for $\text{ic} = 10^5$, it is way larger than the maximum to accept that the data follows a gamma distribution. Therefore, further investigations of the pdf's need to be performed to clarify the underlying probability law.

6 Conclusions and outlook

A numerical study of the standard map M_k (1) for values of the parameter close but larger than Greene's constant has been presented. In particular, we have reviewed the way the standard map dynamics fits within the framework of the Greene-MacKay renormalisation theory for invariant curves of twist maps. The accurate computations performed together with the comprehension of the properties of the renormalisation operator lead to an algorithm that allowed us to compute an approximation, with 21 significant digits, of Greene's constant.

On the other hand, we have explored the phase space near the golden Cantorus of M_k with special emphasis on the evolution of the approximating islands. Moreover, we have presented a detailed study of the escape rates through the golden Cantorus of M_k for values of the parameter close but larger than Greene's constant. The detailed study of the evolution of the approximating islands near the Cantorus we performed might help to explain the periodic fluctuations around the mean inverse potential behaviour of the escape rates one observes as $k \rightarrow k_G$. We have also given evidence of the shape of the periodic function $\langle N_k \rangle (k - k_G)^B$ that has period one in \log_δ scale.

Finally, we would like to comment that the careful numerical exploration of the approximating islands we performed suggests to investigate the transport properties using a nearest neighbour

Markov process with different states (as many as relevant approximating islands appear near the Cantorus). Such approach might help to determine the probability law of escape rates that, as commented, deserves further investigations to be clarified.

A natural question that arises is how the reported results depend on the precise choice of the standard map family (1) for the simulations. The local results concerning the islands near the Cantorus and the local transport properties are expected to hold for other maps provided the last destroyed curve in the local Cantor set of invariant curve has a noble frequency. On the other hand, the global results concerning the mean escape rate might significantly differ for other families of maps. As mentioned in Section 4 one can consider modifications of the standard map with a two harmonic term instead of the $\sin(x)$ term, for which the last RIC can reappear (usually with a different rotation number) once destroyed when changing the perturbation parameter (the k for the standard family M_k here considered) monotonically, see [8, 9, 4, 22]. Also for families like the rational standard map, where $\sin(x)/(1 - \mu \cos(x))$ with $\mu \in [0, 1)$ is considered instead of the $\sin(x)$ term, the results might differ, see [6]. It would be interesting to consider these cases and compare with the results here in future works.

Acknowledgments

This work has been supported by grants PID2019-104851GB-I00 (Spain) and 2017-SGR-1374 (Catalonia). We thank Jaume Timoneda for maintaining the computing facilities of the Dynamical Systems Group of the Universitat de Barcelona, which have been widely used in this work.

References

- [1] Arioli G. and Koch H., The critical renormalization fixed point for commuting pairs of area-preserving maps, *Comm. Math. Phys.* 295(2), 415–429, 2010.
- [2] Batut, C., Belabas, K., Bernardi, D., Cohen, H., and Olivier, M.: *Users' guide to PARI/GP*, <http://pari.math.u-bordeaux.fr/>
- [3] Berretti, A. and Gentile, G., Scaling of the critical function for the standard map: some numerical results, *Nonlinearity* 17(2), 649–670, 2004.
- [4] Calleja, R. and de la Llave, R., A numerically accessible criterion for the breakdown of quasiperiodic solution and its rigorous justification, *Nonlinearity* 23(9), 2029–2058, 2010.
- [5] Chirikov, B. V., A universal instability of many-dimensional oscillator systems, *Phys. Rep.* 52(5), 264–379, 1979.
- [6] Cincotta, P.M. and Simó, C., Global dynamics and diffusion in the rational standard map, *Physica D* 413, 132661, 2020.
- [7] Dana, I. and Fishman, S., Diffusion in the standard map, *Phys. D* 17(1), 63–74, 1985.
- [8] Falcolini C. and de la Llave R., A rigorous partial justification of Greene's criterion *J. Statist. Phys.* 67(3-4), 609–643, 1992.
- [9] Falcolini C. and de la Llave R., Numerical calculation of domains of analyticity for perturbation theories in the presence of small divisors, *J. Statist. Phys.* 67(3-4), 645–666, 1992.
- [10] Figueras, J-Ll., Haro, À. and Luque, A, A Rigorous computer assisted application of KAM theory: a modern approach *Found. Comput. Math.* 17(5), 1123–1193, 2017.

- [11] Golé, C., Symplectic Twist Maps, Global Variational Techniques Advanced Series in Non-linear Dynamics, 18, World Scientific, 2001.
- [12] Greene, J. M., A method for determining stochastic transition. J. Math. Phys. 6(20), 1183–1201, 1979.
- [13] Haydn, N., On invariant curves under renormalisation Nonlinearity 3(3), 887–912, 1990.
- [14] Kadanoff, L. P. and Shenker, S. J., Critical Behavior of a KAM Surface: I. Empirical Results, J. Stat. Phys. 27(4), 631–656, 1982.
- [15] Koch, H., On hyperbolicity in the renormalization of near-critical area-preserving maps, Discrete Contin. Dyn. Syst. 36(12), 7029–7056, 2016.
- [16] de la Llave, R. and Olvera, A., The obstruction criterion for non-existence of invariant circles and renormalization, Nonlinearity 19(8), 1907–1937, 2006
- [17] MacKay, R. S., A renormalisation approach to invariant circles in area-preserving maps, Phys. D 7(1-3), 283–300, 1983. Order in chaos (Los Alamos, N.M., 1982).
- [18] MacKay, R. S., Greene’s residue criterion, Nonlinearity 5(1), 161–187, 1992.
- [19] MacKay, R. S., *Renormalisation in area-preserving maps*, Advanced Series in Nonlinear Dynamics, 6. World Scientific, 1992.
- [20] R. S. MacKay, Existence of invariant circles for infinitely renormalisable area-preserving maps, in Dynamics, games and science. I, 631–636, Springer Proc. Math., 1, Springer, Heidelberg, 2011.
- [21] MacKay, R. S., Meiss, J. D. and Percival, I. C., Transport in Hamiltonian systems, Phys. D 13(1-2), 55–81, 1984.
- [22] Martínez, R. and Simó, C., Invariant manifolds at infinity of the RTBP and the boundaries of bounded motion, Regular and Chaotic Dynamics, 19(6), 745–765, 2014.
- [23] Mather, J. N., Nonexistence of invariant circles, Ergod. Th. & Dynam. Sys. 4(2), 301–309, 1984.
- [24] Mather, J. N., A criterion for the nonexistence of invariant circles, IHES Publ. Math 63, 153–204, 1986.
- [25] Meiss, J. D., Symplectic maps, variational principles, and transport, Rev. Modern Phys. 64(3), 795–848, 1992.
- [26] Meiss, J. D., Thirty Years of Turnstiles and Transport, Chaos, 25(9), 17pp, 2015.
- [27] Miguel, N., Simó, C., and Vieiro, A., Effect of Islands in Diffusive Properties of the Standard Map for Large Parameter Values, Found. Comput. Math. 15(1), 89–123, 2015.
- [28] Olvera, A. and Simó, C., An obstruction method for the destruction of invariant curves. Phys. D 26(1-3), 181–192, 1987.
- [29] Simó, C. and Treschev, D., Evolution of the “last” invariant curve in a family of area preserving maps. Preprint, 1998, see <http://www.maia.ub.es/dsg/1998/index.html>
- [30] Simó, C. and Vieiro, A., Resonant zones, inner and outer splittings in generic and low order resonances of Area Preserving Maps, Nonlinearity 22(5), 1191–1245, 2009.
- [31] Stirnemann, A., Renormalization for golden circles, Commun. Math. Phys. 152(2), 369–431, 1993.
- [32] Stirnemann, A., Towards an existence proof of MacKay’s fixed point, Commun. Math. Phys. 188(3), 723–35, 1997.